Journal of Materials Research and Technology 34 (2025) 880–897

Contents lists available at ScienceDirect

Journal of Materials Research and Technology

journal homepage: www.elsevier.com/locate/jmrt

Inhibiting surface and subsurface damage in ultrasonic vibration-assisted ultraprecision diamond cutting of high-entropy alloy

Yintian Xing [a], Yue Liu [b], Yuhan Li [a], Tengfei Yin [a], Denghui Li [a], Changxi Xue [b], Wai Sze Yip [a,**], Suet To [a,c,*]

[a] State Key Laboratory of Ultra-precision Machining Technology, Department of Industrial and Systems Engineering, The Hong Kong Polytechnic University, Hong Kong, China
[b] Department of Optical Engineering, Changchun University of Science and Technology, Changchun, China
[c] The Hong Kong Polytechnic University Shenzhen Research Institute, China

ARTICLE INFO

Keywords:
Ultrasonic vibration-assisted diamond cutting
Surface damage features
Subsurface microstructure characteristics
High-entropy alloys

ABSTRACT

High-entropy alloys (HEAs) are a potential industrial material for large-scale applications because of their superior physical and chemical attributes. However, owing to the incomplete understanding of the manufacturing mechanism for this material, it is a challenge to realize ultra-precision nanoscale manufacturing of HEAs while preventing surface and subsurface damage. Therefore, in this work, ultrasonic vibration-assisted diamond cutting (UVDC) was utilized to manufacture HEAs workpieces, with the aim of clarifying and revealing the formation mechanisms of high-precision surface integrity. The scientific phenomena of material removal characteristics are explored and investigated, encompassing a range from macroscopic surface overall topography to microscopic subsurface atomic changes. This is achieved through comprehensive comparisons of the workpiece surface, subsurface features, chip morphology, and tool damage in cutting processes with and without high-frequency ultrasonic vibration assistance. Results indicate that the diverse machinability advantages of HEAs in intermittent cutting can effectively inhibit surface and subsurface damage, including better cutting stability, smoother material removal, and lower tool wear. This study enhances the understanding of the high-precision surface formation mechanisms in HEAs by suppressing damage during UVDC, thereby meeting the stringent demands of practical applications.

1. Introduction

Diamond cutting (DC) technology is widely used to obtain nanometer-precision workpiece surfaces, which is applied in the fields of optics, medicine, and microelectronics [1–3]. With the development of materials science, new types of industrial materials, high-entropy alloys (HEAs), have excellent physical and chemical attributes, such as high hardness, superb wear resistance, excellent corrosion resistance, etc., and a diverse array of potential applications, but they generally have poor processability [4,5]. Because HEAs have active transition elements that are prone to affinity reactions with the carbon elements of diamond tools, reducing tool life, it is hard to realize high-precision workpiece surfaces using only diamond-cutting technology [6,7]. Therefore, how to achieve nano-precision workpiece surface quality manufacturing of HEAs through ultra-precision diamond cutting technology has become a challenge.

Ultrasonic vibration-assisted diamond cutting (UVDC) technology has been extensively employed in recent years to manufacture and enhance the precision of workpiece surfaces for materials that are challenging to cut when satisfactory results cannot be obtained through DC technology alone [8–10]. Ultrasonic vibrational machining can improve the machinability of diamond cutting. In terms of tool duration, Song et al. thought that when the cutting time between the diamond tool and the workpiece was less than 0.3 ms, the tool durability could be substantially enhanced through experimental analysis of intermittent cutting of ferrous metal materials [11]. In terms of the cutting force, Niu et al. believed that vibration-assisted machining dramatically decreased the average cutting force, thereby improving the machinability during

* Corresponding author. State Key Laboratory of Ultra-precision Machining Technology, Department of Industrial and Systems Engineering, The Hong Kong Polytechnic University, Hong Kong, China.
** Corresponding author.
E-mail addresses: lenny.ws.yip@polyu.edu.hk (W.S. Yip), sandy.to@polyu.edu.hk (S. To).

https://doi.org/10.1016/j.jmrt.2024.12.124
Received 3 October 2024; Received in revised form 25 November 2024; Accepted 16 December 2024
Available online 18 December 2024

the material removal [12]. In terms of cutting stability, Xiao et al. deemed that even if a larger tool radius was used for processing, vibration-assisted cutting technology still effectively suppressed chatter and improved cutting stability [13]. In terms of workpiece surface quality, Xing et al. considered that intermittent cutting enhanced the workpiece machining quality of metal materials and reduced surface damage [14].

Based on the above manufacturing advantages, many researchers have conducted various research on UVDC manufacturing technology. Regarding the study of the cutting mechanism, Chen et al. analyzed the removal process of materials during vibration cutting of aluminum-based silicon carbide [15]. Zhang et al. studied the cooling mechanism during vibrational machining [16]. Regarding the tool wear mechanism, Pan et al. studied the wear of diamond tools in cutting tungsten-heavy alloy and found that intermittent cutting effectively reduced the diamond graphitization [17]. Zhang et al. found that sub-millisecond oxide formation was an important factor for the rapid wear of diamond tools while processing ferrous materials, and vibration cutting can inhibit the occurrence of this phenomenon [18]. Regarding the research on machining parameter optimization, Nath et al. found a relationship among vibration frequency, vibration amplitude, and nominal cutting speed, and analyzed their impact on workpiece surface quality, cutting force and tool wear [19]. Regarding the advancement of new ultrasonic vibration devices, Wang et al. studied a non-resonant elliptical vibration device to achieve texture structure processing on brittle materials, expanding the manufacturing method of microstructures using discontinuous cutting technology [20]. Duan et al. developed a three-dimensional vibrational cutting device and proved that the application of Lissajous vibration trajectory machining can further reduce cutting forces by experimental verification [21]. Regarding the research on simulation, Patil et al. simulated the intermittent cutting technology of Ti6Al4V material by finite element simulation technology and explained the processing mechanism during the material removal process at the macro level [22]. Wang et al. applied molecular dynamics to simulate the elliptical vibration-assisted machining process of tungsten alloy, explaining the impact of vibration processing on the internal atomic level changes of the material at the microscopic level [23].

From the perspective of material processing, UVDC machining technology primarily focuses on two major categories of materials: ferrous metals and fragile materials. Ferrous metals include iron-based materials [24,25], titanium-based materials [26,27], nickel-based materials [28,29], and tungsten-based materials [30,31], among others. Current research on these materials aims to uncover the mechanisms behind rapid tool wear, improve the machining precision of workpieces, and analyze the characteristics of material removal. Fragile materials can be categorized further into two subcategories: hard-brittle materials (such as WC [32], SiC [33], ZrO_2 [34], BK7 [35], and Si [36]) and soft-brittle materials (such as GaF_2 [37], KDP [38], and ZnSe [39]). Research on the intermittent cutting of fragile materials is currently centered around understanding mechanisms of fracture generation, precisely controlling the brittle-ductile transition, and achieving high-precision manufacturing of complex or free-form surfaces.

Furthermore, with the progress in material analysis techniques, a growing number of researchers are applying advanced characterization techniques to analyze and explore the microscopic phenomenological characteristics of workpiece materials. This approach aims to further explore and uncover the fundamental mechanisms of material changes during processing. Saito et al. utilized X-ray diffraction (XRD) technology to study the elements composition of the workpiece surface after vibration processing of steel materials and discussed the impact of alloy elements on the damage and wear of diamond tools [40]. Chen et al. employed Raman spectroscopy technology to analyze single-crystal silicon chips after vibration cutting and deliberated the affecting of processing parameters on the phase transformation of silicon [41]. Wang et al. used Electron Backscattered Diffraction (EBSD) technology to characterize processed tungsten alloys and compared the effects of intermittent cutting and continuous machining on the regeneration of grain boundaries at grain boundaries in the crystal refinement layer [42]. Peng et al. used Transmission Electron Microscopy (TEM) measurement technology to analyze the evolution gradient characteristics of the subsurface microstructure of titanium alloy materials after vibration processing and compared the damage situation with and without assistance machining [43].

At present, some researchers are trying to conduct research on ultraprecision vibration-assisted processing technology for HEAs materials. Luo et al. used molecular dynamics simulation technology to simulate the UVDC process of HEAs workpieces, and explored the cutting temperature, cutting force, and chip deformation [44]. Zhang et al. carried out a preliminary investigation into the machinability of HEAs materials when subjected to high-frequency vibration-assisted cutting [45]. However, these studies are still insufficient for a deep understanding of the macroscopic surface features and microscopic subsurface microstructure characteristics formed during the material removal process when cutting HEA workpieces using UVDC technology. A comprehensive investigation and exploration of the phenomenological aspects of UVDC processing of HEAs to reveal the underlying machining mechanisms remains a significant research gap.

This research endeavor aims to deepen our understanding and uncover the mechanism underlying the removal of material during the formation of high-precision surfaces when UVDC technology is used to process HEAs workpieces. The in-depth scientific phenomena of material removal characteristics are explored and investigated, ranging from macroscopic overall surface topography to microscopic subsurface atomic changes. The machinability advantages of HEAs in intermittent cutting are obtained through in-depth comprehensive comparisons of the workpiece surface, subsurface features, chip morphology, and diamond tool wear in cutting with and without ultrasonic vibration assistance. The research results help to further understand the essential material removal mechanisms in ultraprecision surface formation by analyzing and investigating the inhibition of surface and subsurface damage for HEAs processed by high-frequency UVDC processing technology.

2. Processing principle of UVDC

Fig. 1 illustrates the overall layout of UVDC machining technology and the processing principle behind HEAs removal. The ultrasonic-assisted machining apparatus is mounted on the B-axis platform, which moves following the Z-axis direction. The HEAs materials, which are held in the fixture, are secured to the rotating spindle as illustrated in Fig. 1 (a) and 1 (b). The diamond cutter equipped in this apparatus is connected to the ultrasonic vibration system through transducers to ensure the effective transmission of ultrasonic energy and stable operation. Fig. 1 (d) displays the geometric features of the diamond tool in this work, including rake face, flank face, cutting edge, tool radius, and tool handle. Additionally, the UVDC processing technology causes the diamond tool to undergo rapid, repetitive periodic harmonic motions, resulting in material removal from the workpiece surface [35]. The repetitive engagement and disengagement of the tool with the workpiece result in a transient material removal time within each cycle. In this study, the ultrasonic vibration-assisted device which is supported by Son-X company operates at frequencies exceeding 100 kHz, resulting in an actual cutting time of only 20–40% per cycle, equivalent to 2–4 μs [46]. This instantaneous cutting process does not provide sufficient time for chemical affinity effects, for instance, the generation of graphitization phenomenon, to occur throughout the engagement of the tool with the workpiece. Consequently, this protects the tool and extends its lifespan. Furthermore, the movement path of the diamond tool in the vibration process follows an arc-shaped cutting path that is approximately linear. During a vibration cycle, the tool advances following the red line for cutting and then reverses following the blue line for retraction in Fig. 1(c). The reason for the movement trajectory is that the

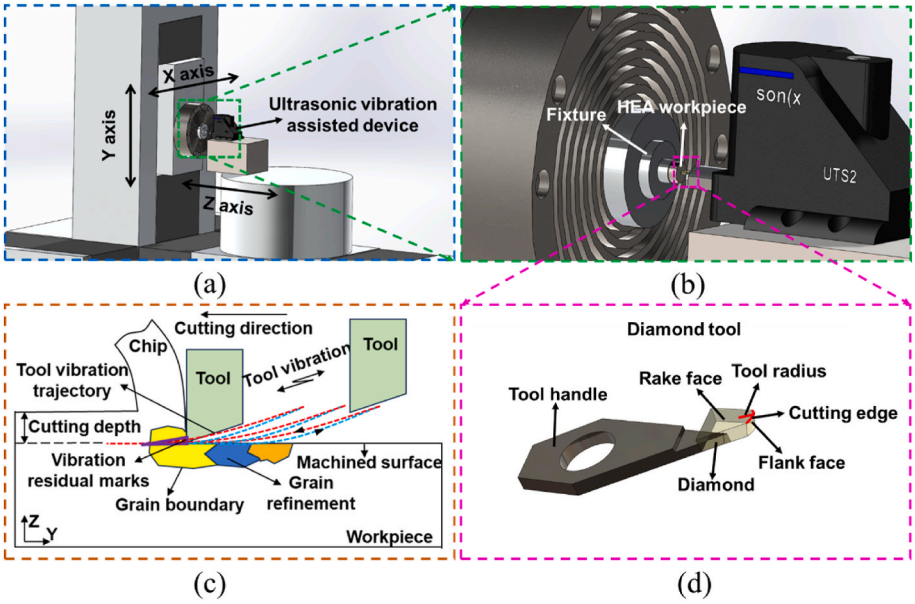

Fig. 1. Schematic diagram of UVDC processing of HEAs. (a) Overall layout of machining device; (b) Particulars of the cutting process; (c) Process of removing materials in intermittent cutting; (d) Diamond tool.

vibration is not only longitudinal vibration along the Y-axis direction but also transverse vibration along the Z-axis direction. In this stable cutting process, their amplitude ratio is 5:1 [47]. Moreover, there is a 180-degree phase difference between the transversal and longitudinal vibrations at the tooltip. Because of this arc-like vibration trajectory, as the cutting tool engages and disengages with HEAs during each processing cycle, multiple residual traces are left on the machined workpiece [48]. According to the preceding analysis, the movement path of the diamond tool tip can be described as:

$$\begin{cases} Y_v^{(t)} = A_y \sin(2\pi ft + \varphi_y) \\ Z_v^{(t)} = A_z \sin(2\pi ft + \varphi_z) \end{cases}, \tag{1}$$

where A_y and A_z are the amplitudes, f is the frequency, φ_y and φ_z are the phases, and t is the cutting time. Furthermore, in this work, the study displays a frequency of approximately 103 kHz, with amplitudes measuring roughly 1000 nm in the cutting direction and 200 nm in the cutting depth direction.

During high-frequency vibration cutting, although the nominal cutting speed remains constant, the actual materials removal rate varies cyclically. As the machining tool cuts through the workpiece material, the actual removal rate begins to fluctuate, initially increasing and then decreasing. While the actual cutting speed gradually reduces to the decoupling point, the cutter and the workpiece material begin to separate from each other and move in opposite directions relative to the workpiece movement direction. Hence, the actual cutting speed can be formulated as:

$$V_{CS}^{(t)} = V_W^{(t)} + V_{Tool}^{(t)} = V_W^{(t)} + \{2\pi fA_y \cos(2\pi ft + \varphi_y)\}\vec{i} + \{2\pi fA_z \cos(2\pi ft + \varphi_z)\}\vec{j}, \tag{2}$$

where $V_W^{(t)}$ is the nominal cutting speed.

In a vibration cycle, it is assumed that the diamond tool begins at the origin of the ultrasonic vibration system, marking the start of the first cycle. Initially, there is no direct contact between the tool and the workpiece being processed. As the tool begins to move and makes contact with the workpiece for the first time, both move toward each other until they reach maximum displacement. This process can be described as follows:

$$A_y \sin(2\pi ft_C) + V_W^{(t)}(T/4 - t_C) = A_y, \tag{3}$$

where t_S is the contact time point between the tool and the workpiece, which can be obtained based on Taylor expansion formula:

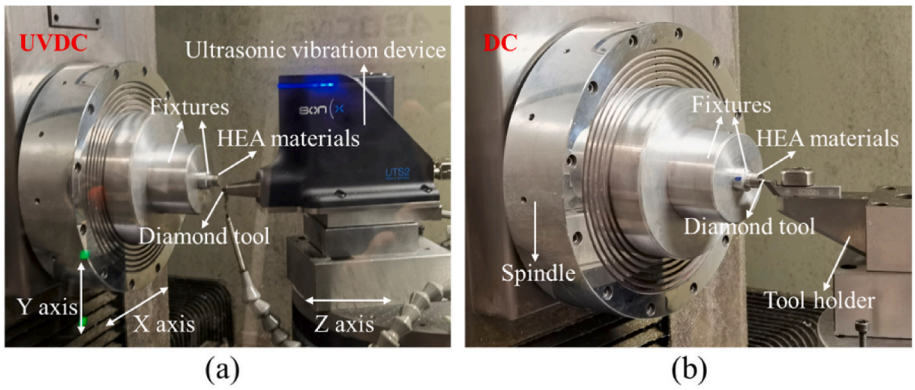

Fig. 2. Experimental setup of UVDC and DC. (a) UVDC; (b) DC.

$$t_C = \frac{\left(A_y + \frac{V_W^{(t)} T}{4}\right)}{\left(2\pi f A_y - V_W^{(t)}\right)}. \tag{4}$$

During the period from when the tool starts to move toward the workpiece until the tool changes direction of movement, the length of material removed $S_C^{(t)}$ can be expressed as:

$$S_C^{(t)} = S_{CT}^{(t)} - S_{CW}^{(t)} = A_y - A_y \sin\left(2\pi f\left(\frac{A_y + \frac{T}{4}V_W^{(t)}}{2\pi f A_y - V_W^{(t)}}\right)\right) + V_W^{(t)}\left(\frac{\pi}{4} - \frac{A_y + \frac{T}{4}V_W^{(t)}}{2\pi f A_y - V_W^{(t)}}\right), \tag{5}$$

where $S_{CT}^{(t)}$ and $S_{CW}^{(t)}$ are the distances moved by the tool and the workpiece respectively.

When the tool and workpiece separate, the relative speed between them is zero. At this time, the relationship between the tool and the workpiece along the cutting direction is expressed as:

$$2\pi f A_y \cos(2\pi f t_S) + V_W^{(t)} = 0, \tag{6}$$

where t_S is the separation time point between the tool and the workpiece, which can be obtained:

$$t_S = \frac{1}{2\pi f}\arccos\frac{-V_W^{(t)}}{2\pi f A_y}. \tag{7}$$

During the period when the tool and the workpiece move in the same direction until they are separated, the material removal length $S_S^{(t)}$ is

$$S_S^{(t)} = S_{SW}^{(t)} - S_{ST}^{(t)} = V_W^{(t)}\left(\frac{\arccos\left(\frac{V_W^{(t)}}{2\pi A_y f}\right)}{2\pi f} - \frac{T}{4}\right) - A_y + A_y \sin\left(2\pi f\left(\frac{\arccos\left(\frac{V_W^{(t)}}{2\pi A_y f}\right)}{2\pi f} - \frac{T}{4}\right)\right), \tag{8}$$

where $S_{ST}^{(t)}$ and $S_{SW}^{(t)}$ are the distances moved by the tool and the workpiece respectively.

Therefore, in a single vibration cycle, the length S of material removed can be obtained:

$$S = S_C^{(t)} + S_S^{(t)} = A_y - A_y \sin\left(2\pi f\left(\frac{A_y + \frac{T}{4}V_W^{(t)}}{2\pi f A_y - V_W^{(t)}}\right)\right) + V_W^{(t)}\left(\frac{\pi}{4} - \frac{A_y + \frac{T}{4}V_W^{(t)}}{2\pi f A_y - V_W^{(t)}}\right) + V_W^{(t)}\left(\frac{\arccos\left(V_W^{(t)}/2\pi A_y f\right)}{2\pi f} - \frac{T}{4}\right) - A_y + A_y \sin\left(2\pi f\left(\frac{\arccos\left(V_W^{(t)}/2\pi A_y f\right)}{2\pi f} - \frac{T}{4}\right)\right). \tag{9}$$

3. Experiment and measurement

The experiments are processed on an ultra-precision machine tool with UVDC and DC machining respectively, illustrated in Fig. 2(a) and (b). The ultrasonic device with vibration frequency 103 KHz and amplitude 1 μm is set on the rotating platform, translating in the Z-axis direction in linear mode. The ultrasonic equipment is constituted by the longitudinal transducer and the curved sonotrode, driving the diamond tool to cut the workpiece material with high-frequency vibration. Two natural diamond tools of the same type are used for experiments in UVDC and DC processing. In the experiments, the diamond cutting tools feature a radius measuring approximately 1 mm, along with rake and relief angles set at 0° and 15°. Samples of HEAs (CrMnFeCoNi) have a radius of 5 mm and a thickness of 10 mm, which are pretreated by the electrical discharge machining to ensure the parallelism of workpieces. The selected HEAs are the crystal structure of face-center-cubic (FCC) in this research. The content and distribution of the composition elements in the unprocessed materials are approximatively proportional and equational by the measurement of EDS mapping, as shown in Fig. 3(a)

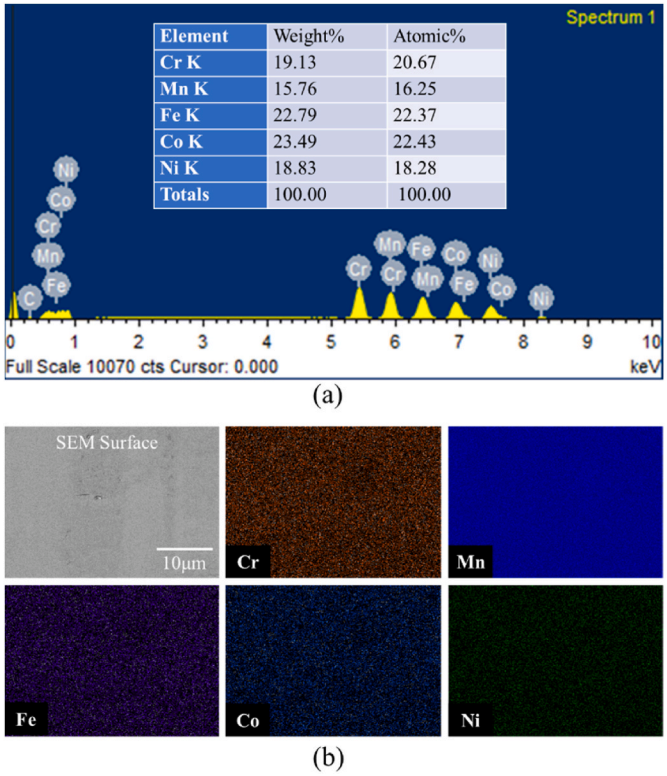

Fig. 3. EDS mapping of CrMnFeCoNi HEA sample. (a) Content of each element; (b) Distribution of each element.

Table 1
Experimental machining parameters.

	Nominal cutting speed (m/min)	Cutting depth (μm)	Feeding distance (μm/time)	Vibration frequency (KHz)	Vibration amplitude (μm)
UVDC	1	10	2	103.54	1
DC	1	10	2	\	\

and (b). The workpiece materials are stuck to the fixture. Also, before actual processing, other diamond tools are used for secondary pre-treatment to ensure the flatness of the workpiece material, avoiding under-cutting and over-cutting phenomena, and ensuring the stability of the sample removal amount. Furthermore, to more intuitively display the variations in the surface and subsurface characteristics of the materials after cutting, the straight groove is processed and formed through linear cutting. The relevant processing parameters are displayed in Table 1. Besides, dry-cutting processing without cooling liquid is executed to collect chips and avoid unnecessary interference.

After the cutting experiments of UVDC and DC, a variety of measurement and characterization techniques are employed to explore the surface and subsurface microstructural features for the workpiece materials. The white light interferometer is used to measure and digitize the three-dimensional morphology and surface roughness. The atomic force microscope (AFM) is utilized to investigate the surface pattern of micro-morphology. A field emission scanning electron microscope (SEM) is applied to observe the surface damage feature, chip formation, and diamond tool wear. An X-ray diffraction analysis (XRD) is operated to survey the variation of crystal structure after UVDC and DC machining. Energy-dispersive X-ray spectroscopy (EDS) is applied to map and analyze the elemental content and distribution before and after manufacturing. The focused ion beam (FIB) is applied to create samples for subsequent measurements. A spherical aberration-corrected transmission electron microscope (ACTEM) is used to measure the subsurface microstructure characterizations.

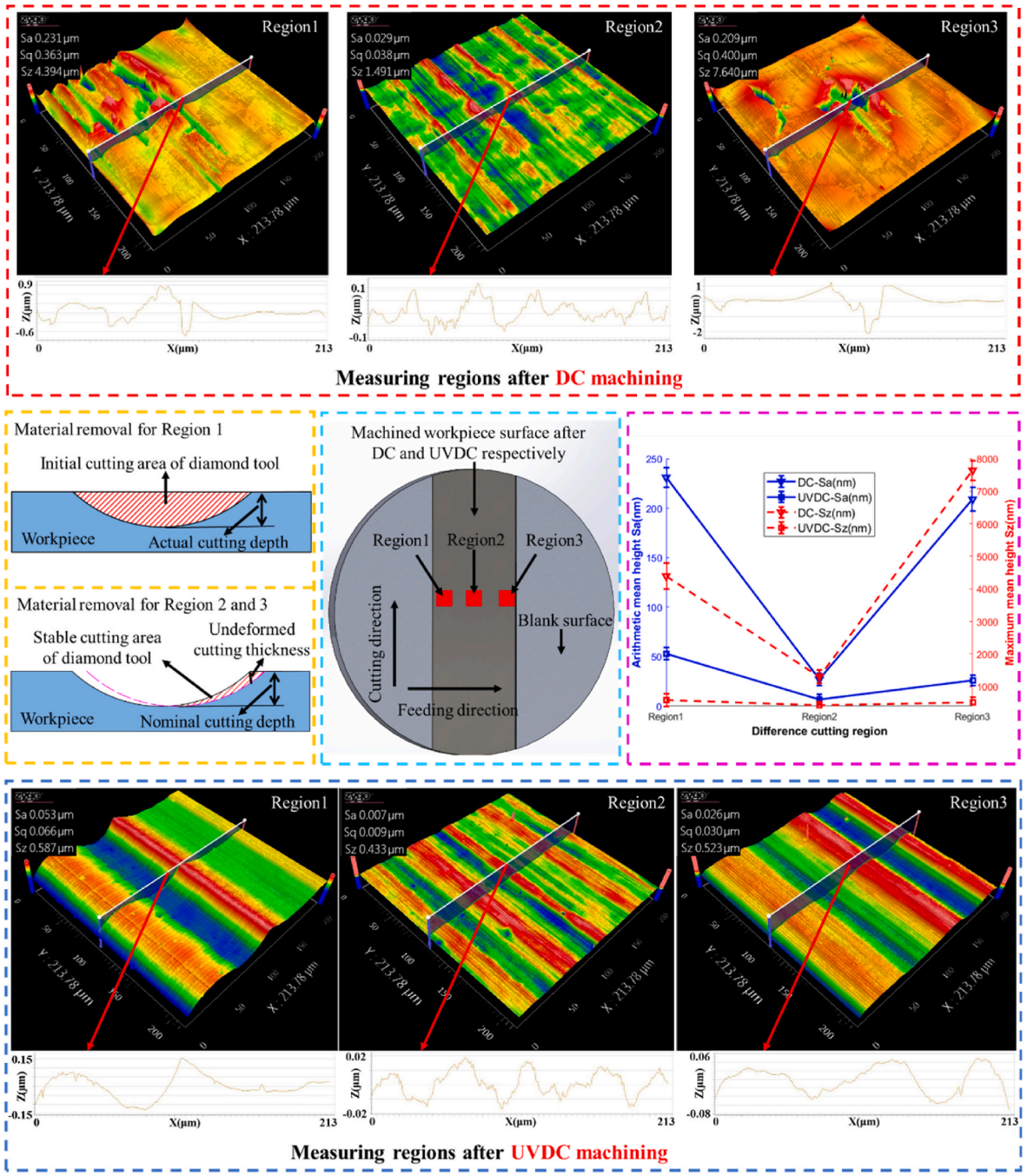

Fig. 4. The three-dimensional topographies and surface roughness of the machined workpiece after DC and UVDC in cutting-in region, stable cutting region and cutting-out region measured by white light interferometry.

4. Results and discussion

4.1. Surface topography features

Three-dimensional surface topography and surface quality of the machined workpiece after DC and UVDC are surveyed using a white light interferometer. Since the straight groove surface is processed by linear cutting of the diamond tool, three regions of groove surfaces are measured separately, namely Region 1 in the initial cutting area, Region 2 in the stable cutting area, and Region 3 in the final cutting area, as shown in Fig. 4. For the initial cutting area of material removal, the machining result of Region 1 is the area with the largest amount of material removal since the nominal cutting depth is same as the actual cutting depth when the diamond tool first cuts. After DC processing, the obvious tearing phenomenon occurs on the machined workpiece surface. This result shows that larger material removal makes the shear stress applied by the diamond tool on the HEAs workpiece more concentrated, causing the local stress to exceed the yield strength of HEAs and trigger the occurrence of cracks. When the intermittent cutting is applied, there is no obvious surface tearing in the initial cutting area, but the chatter phenomenon occurs. For stable cutting regions of material removal, the amount of material removed is significantly smaller than the initial cutting area, which is no longer evaluated by the nominal cutting depth but by the undeformed cutting thickness. After DC machining, the surface roughness Sa and Sz values are 29 nm and 1.491 μm, respectively. After UVDC machining, the surface roughness Sa and Sz value are improved to 7 nm and 433 nm, respectively. This result shows that UVDC processing can obviously increase the surface roughness and decrease the local height difference compared with DC processing. For the final cutting area of material removal, the surface to be measured is the arc-shaped machined surface since the tool does not perform further cutting. Different from the measurement results in the stable cutting area, this area can directly observe the surface quality after cutting the undeformed chip thickness. For DC machining, surface cracks can still be observed even though the amount of material removal has been reduced. This phenomenon shows that direct cutting of HEAs with diamond tools is prone to surface damage. This damage can either be carried away with the chip in the next feeding cutting, or it remains on the workpiece due to excessive fracture depth [36]. For UVDC processing, there is still no obvious damage to the workpiece surface, and the chatter phenomenon disappears compared to the initial cutting area. In addition, whether it is DC processing or UVDC processing, the initial machining area exhibits the poorest surface quality, and the stable cutting area demonstrates the highest surface quality based on a comprehensive comparison of three areas, namely Region 1, 2, and 3. Also, UVDC processing results are all better than DC processing results in any area due to intermittent cutting characteristics. The processing feature of high-frequency micro-displacement between the diamond tool and the workpiece alters the friction characteristics at the cutting interface, reduces the cutting force required for material removal, and enhances the uniform distribution of shear stress [8,14,28]. Therefore, this process improves the surface quality of the workpiece and reduces its roughness.

SEM measuring technology is used to more intuitively observe the morphology characteristics of the machined surface processed by DC and UVDC in Figs. 5 and 6 respectively. Also, the stable cutting areas are selected as the measuring positions to show the effect of different processing technologies on HEAs and avoid unnecessary interference. After DC processing, there are various damage types on the machined surface in Fig. 5 (a). For Region A, a large dimple remains on the workpiece materials as shown in Fig. 5 (b). Through magnified observation in Fig. 5 (c), the pit displays a fracture trend in Region B. This phenomenon occurs because HEAs have low plastic deformation and thermal conductivity. As a result, the instantaneous stress concentration can exceed the material strength limit during continuous cutting, ultimately leading to fracture [49]. In Region C and partially magnified Region D, strong friction marks can be observed in Fig. 5(d) and (e), indicating that severe friction behavior and trace amounts of burning occur in local areas [50]. During the continuous cutting process, a significant amount of mechanical energy is transformed into thermal energy, but uneven heat concentration can cause the occurrence of strong friction because of the worse heat conductivity of the HEAs workpiece. Moreover, obvious scratching damage not only appears on Region E as shown in Fig. 5 (f) but also can be observed almost everywhere by DC processing.

After UVDC processing, the features of the workpiece surface can be observed in Fig. 6. There are two main surface characteristics on the workpiece surface, namely circular holes and vibration marks. For the circular holes observed in Fig. 6(a) and (b), their shapes are regular and

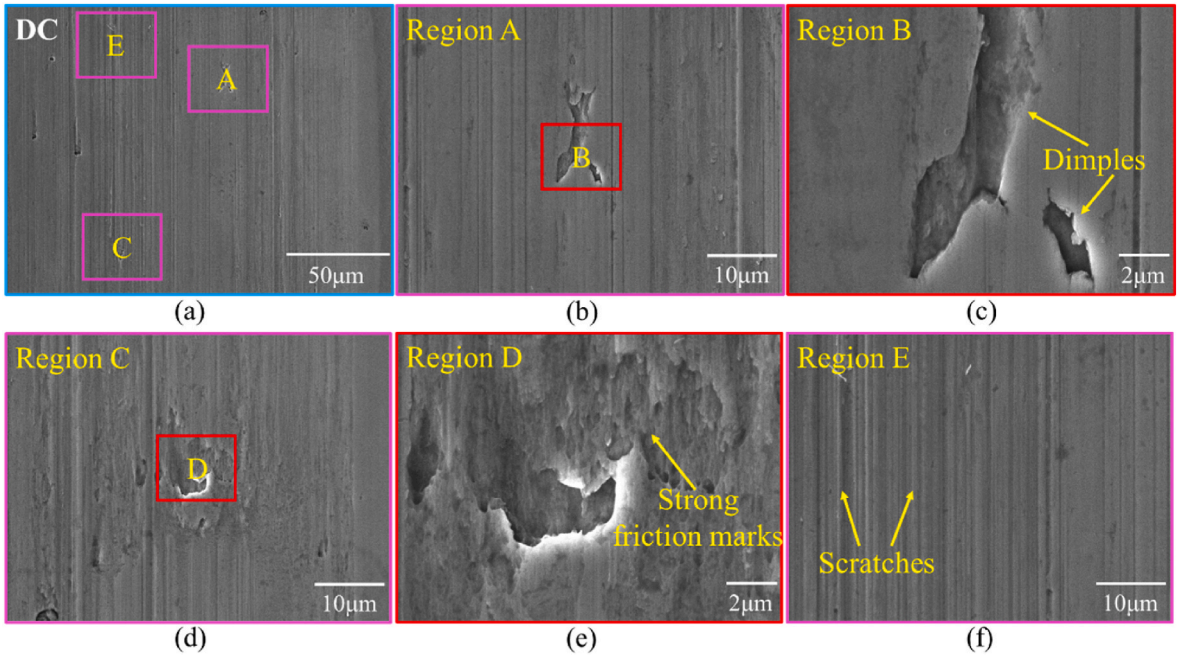

Fig. 5. Surface damage features after DC.

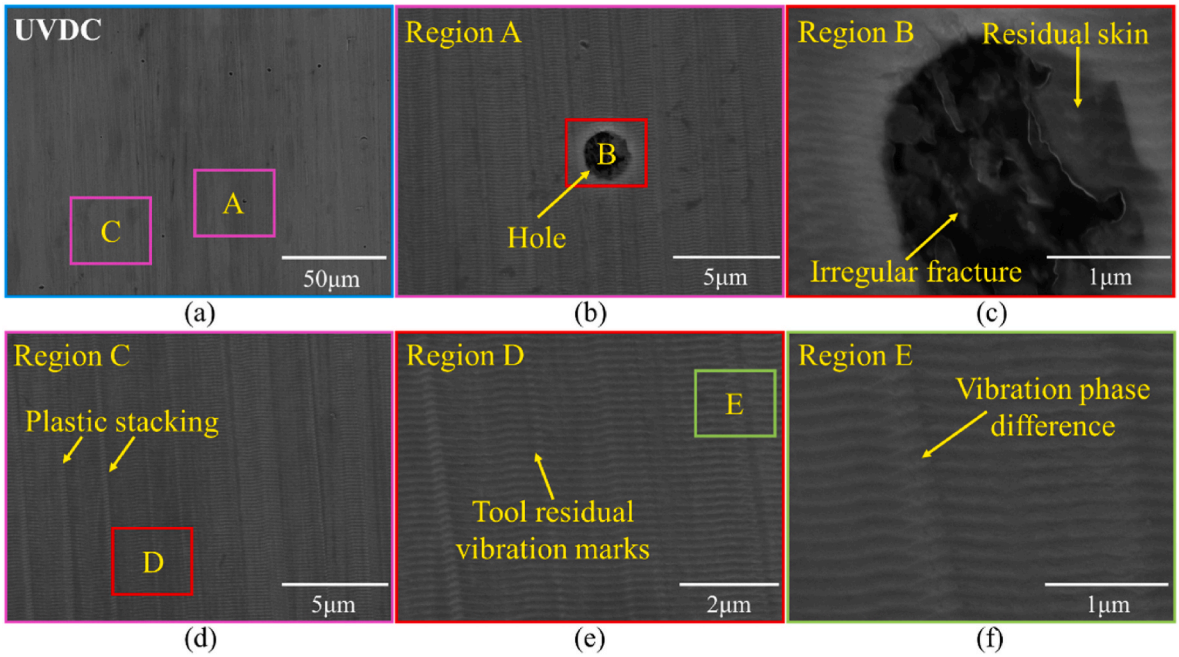

Fig. 6. Surface damage features after UVDC.

deep, which is different from the fracture characteristics of pits after DC processing. In Fig. 6 (c), the surface residual skin left after processing can still be observed through the partial magnification of the cavity in Region B. Also, the interior of the cavity exhibits irregular fracture features. The reason for this phenomenon may be that the whole crystal of HEAs is pulled out of the workpiece materials during the intermittent machining process because of the pushing and stretching effects of the cutting edge. In addition, the vibration marks that are observed in Fig. 6 (d)–(f) are generated because the movement trajectory of the diamond tool in UVDC technology is approximately linear elliptical vibration as shown in Fig. 1 (c), thus leaving residual marks. Each time the diamond tool passes through a vibration cycle, it leaves a vibrative trace until the end of the manufacturing [48]. Furthermore, the intermittent cutting of UVDC technology not only leaves vibration marks along the direction of cutting depth but also leaves marks of material plastic stacking along the tool edge, which is akin to the result of DC processing in Fig. 6 (d) [51, 52]. The workpiece materials begin to deform plastically and flow laterally along the tool side due to the squeezing and shearing effects of the diamond tool during the cutting process, forming the plastic side flow phenomenon [14]. Besides, the vibration residual traces of two adjacent linear cuts intersect with each other as shown in Fig. 6 (f). The result of this vibration phase difference value shows that although the vibration frequency is as high as 103 KHz, UVDC processing of HEAs is still stable cutting, and the plastic deformation ability is improved. By comprehensively comparing the machining results of the two processing technologies, the surface quality of the HEAs after UVDC exhibits a significant improvement compared to DC, and the obvious surface damage almost disappears. The results indicate that intermittent cutting technology for manufacturing HEAs can improve cutting stability, enhance ductile processing capabilities, and optimize surface morphology.

AFM technology is used to conduct measurements to further observe the microscopic morphology features of the machined workpieces after DC and UVDC processing in Fig. 7. The measurement position range of 2 μm × 2 μm is randomly selected in the stable cutting area in Region 2. For the measuring result of DC processing, irregular surface

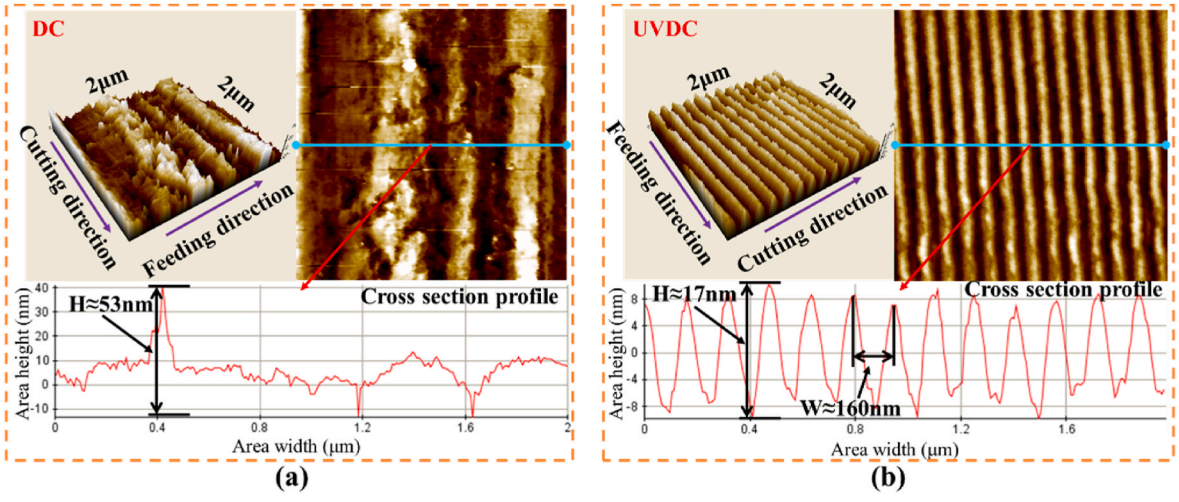

Fig. 7. The local surface characteristics with and without vibration cutting. (a) DC; (b) UVDC.

microtopography can be observed, and disordered tiny peaks and valleys are noticed on the workpiece surface where the local drop height is about 53 nm by surveying the cross-sectional profile in Fig. 7(a). This result certifies again that continuous DC of HEAs has poor cutting stability and makes it difficult to achieve a flat and smooth surface. For the measuring result of UVDC processing, jagged and uniform vibration residual marks are seen and observed by measurements of cross-sectional profiles in Fig. 7 (b). The height and width of the peak and valley morphology generated in one vibration cycle are approximately 17 nm and 160 nm respectively. The results show that intermittent interaction and detachment between the cutter and the workpiece significantly improve the stability and predictability of HEAs removal.

4.2. Subsurface microstructure characteristics

The characteristics of the microstructure located beneath the workpiece surface for HEAs after DC and UVDC machining are observed and measured from microstructure gradient evolution to atomic arrangement features by ACTEM. The changes in subsurface gradient after mechanical processing are categorized into three distinct layers: the recrystallization layer, the transition-crystal layer, and the matrix layer. In this study, the recrystallization layer and crystal transition layer are separately discussed in detail concerning the effects of different processing techniques on microstructural evolution, as illustrated in Figs. 8–12.

Fig. 8 (a) shows the overall trend of microstructure evolution through DC processing. Fig. 8 (b) presents the selected area electron diffraction (SAED) pattern in the recrystallization layer. Nanocrystals and equiaxed crystals can be found in the recrystallized layer in Fig. 8 (c). The crystals of the original material undergo a process of fragmentation, nucleation, growth, and deformation under the influence of mechanical load and strong friction of the diamond tool, and eventually accumulate, forming a recrystallization layer [53,54]. Since a new crystal nucleus needs to be accompanied by the elimination of

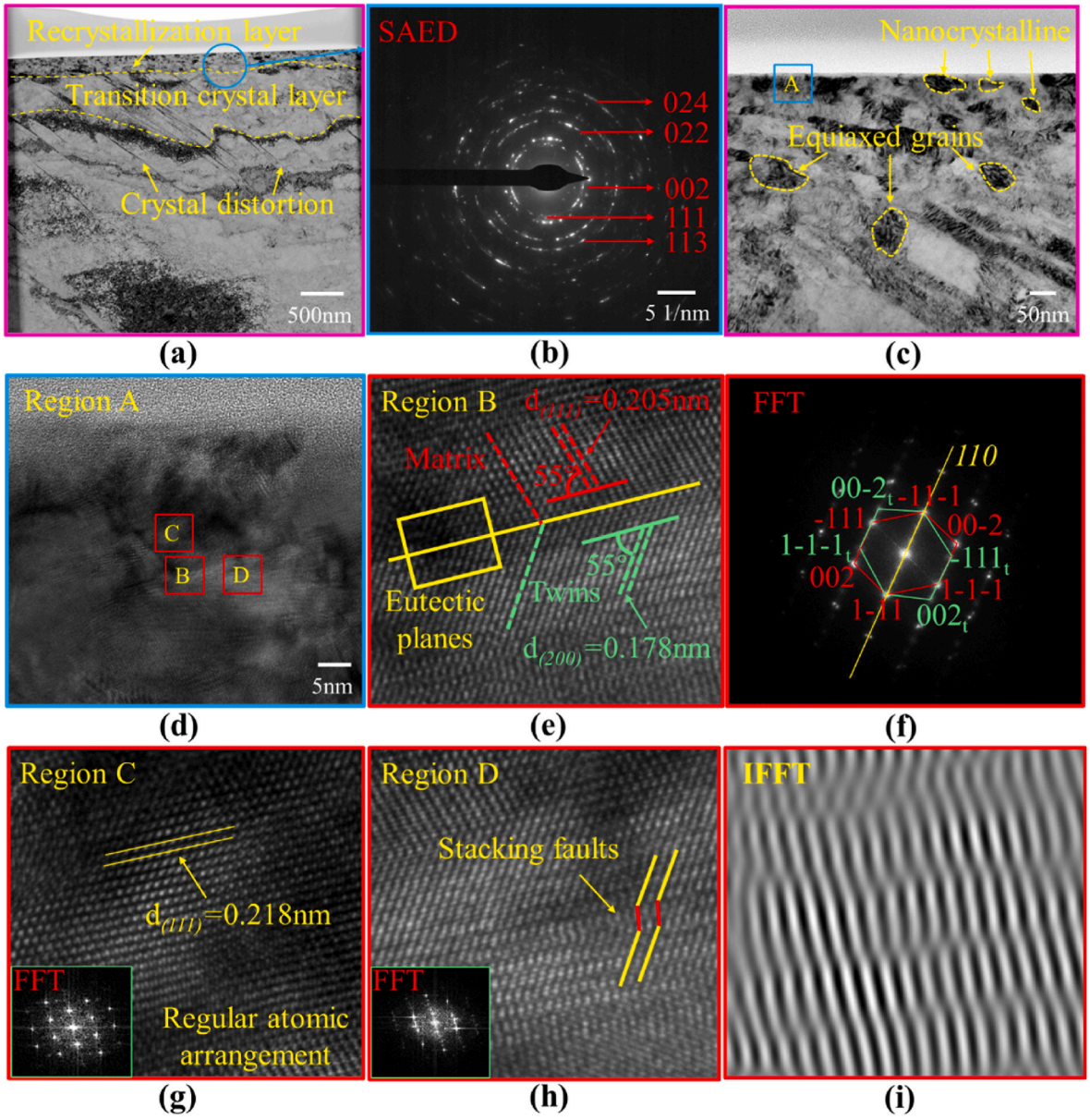

Fig. 8. Microstructure characteristics of recrystallization layer for the machined workpiece subsurface after DC; (a) Microstructure gradient variation; (b) SAED of the selected area in (a); (c) Nanocrystalline in the recrystallized layer; (d) Region A; (e) Twin structure in Region B; (f) FFT pattern in Region B; (g) Region C; (h) Stacking faults structure in Region D; (i) IFFT pattern in Region D.

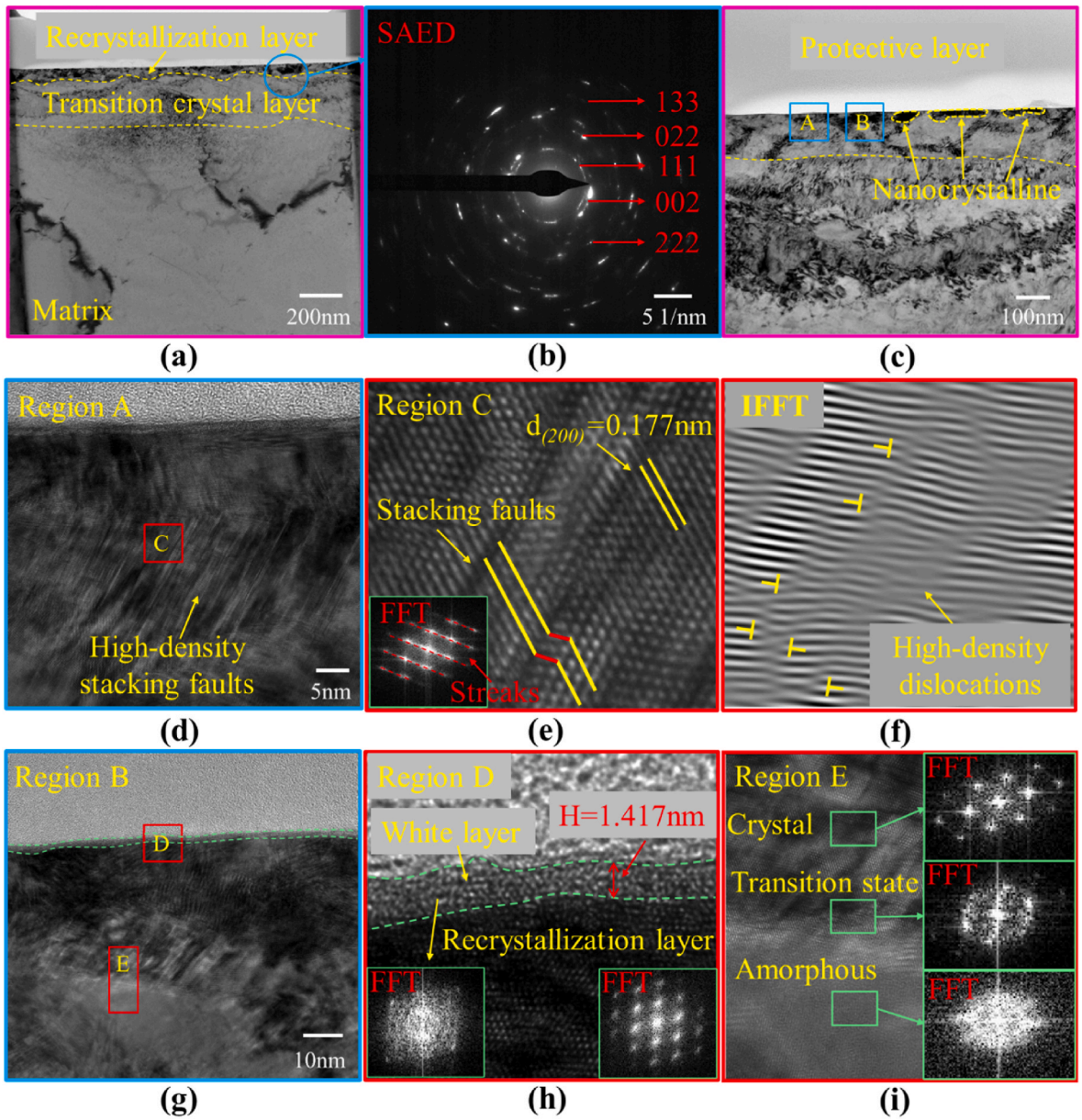

Fig. 9. Microstructure characteristics of recrystallization layer for the machined workpiece subsurface after UVDC. (a) Microstructure gradient variation; (b) SAED of the selected area in (a); (c) Nanocrystals in the recrystallized layer; (d) Region A; (e) Stacking faults structure in Region C; (f) IFFT patten in Region C; (g) Region B; (h) White layer phenomenon in Region D; (i) Region E.

dislocations and the migration of sub-grain boundaries during the dynamic recrystallization process, the atoms inside the newly formed nanocrystals rearrange themselves to create characteristics different from those of the original crystal in Fig. 8 (d). Furthermore, the deformation twin structure is observed in Region B in Fig. 8 (e), which can be confirmed by the characteristic structure of the Fast Fourier Transform (FFT) image in Fig. 8 (f). Also, the angle of misorientation between the matrix and the twins is 55°, and their interplanar spacing is 0.205 nm and 0.178 nm respectively. The existence of the twin structure indicates that unstable stress concentration exists during continuous diamond cutting of HEAs and leads to induced twin deformation, prompting the crystal to continue sliding along the stress direction [9,55].

In Region C, a regular crystal arrangement, exhibiting an interplanar spacing of 0.218 nm, can be observed and confirmed by FFT images in Fig. 8 (g). Moreover, the crystal structure in the recrystallization layer after DC processing still retains the FFC structure, indicating that mechanical processing does not change the original structural properties of the HEAs. In Region D, Fig. 8 (h) shows the stacking fault structure can be observed and confirmed by the feature of elongated diffraction fringes in the FFT image. In the Inverse Fast Fourier Transform (IFFT) image of Region D, the periodic polyline segment features in the spatial domain further verify the discontinuous stacking fault structure characteristics of atomic arrangement in Fig. 8 (i). Since HEAs have a special structure in which multiple elements coexist, stacking fault characteristics can occur in newly formed grain boundaries and crystals, especially during the transition from sub-grain boundaries to high-angle grain boundaries during the dynamic recrystallization process.

The microstructure gradient evolution after UVDC processing is shown in Fig. 9 (a), which is divided into four parts, namely the white layer, the recrystallization layer, the crystal transition layer, and the matrix. In the recrystallized layer after UVDC processing in Fig. 9 (b), the diffraction peaks of the rings vary in intensity compared to that after DC processing in Fig. 8 (b). This result indicates that the uniformity of grain size after UVDC processing is lower than that observed after DC

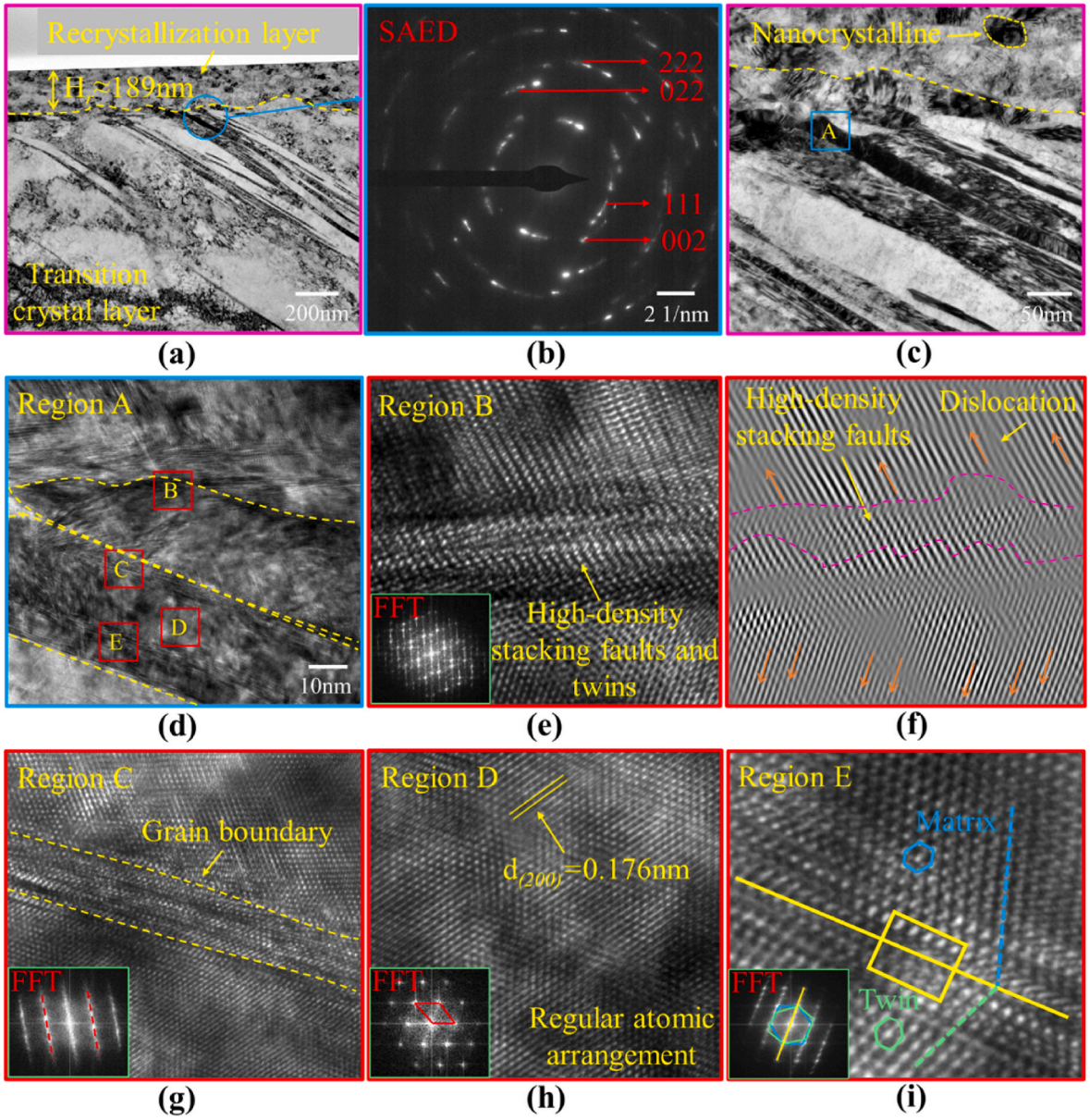

Fig. 10. Microstructure characteristics of the subsurface transition-crystal layer for the machined workpiece after DC. (a) Microstructure gradient variation; (b) SAED of the selected area in (a); (c) Transition-crystal layer; (d) Region A; (e) Region B; (f) IFFT pattern in Region B; (g) Region C; (h) Region D; (i) Region E.

processing. In Fig. 9 (c), the grains resulting from dynamic recrystallization are very fine, with some of them being elongated. Furthermore, in Region A, the inside of the nanocrystal shows high-density stacking faults as shown in Fig. 9 (d), which is different from the structural changes inside the nanocrystal after DC machining in Fig. 8 (d). In the partially enlarged area C, stacking fault characteristics can be observed in Fig. 9 (e), indicating a lattice spacing of 0.177 nm. Furthermore, as depicted in Fig. 9 (f), the IFFT pattern of this region reveals a large concentration of edge dislocations. High concentrations of dislocations and stacking fault defects usually limit the dynamic recovery of the material under high deformation rate loads, thus enhancing the mechanical strength of the workpiece material [56].

Besides, in Region B, two types of amorphous structures appear in the recrystallization layer in Fig. 9 (g). In Region D, the white layer phenomenon occurs on the surface beneath the workpiece, at the top of the recrystallized layer, and its thickness is only about 1.417 nm in Fig. 9 (h). Based on the characteristic observation of the FFT pattern, there is an obvious amorphous phase in the white layer, while an obvious crystalline state appears in the recrystallization layer. The white layer is primarily attributed to the intense cutting heat generated by the severe friction between the tool and the workpiece, coupled with the high shear strain experienced during material removal. This combination of factors leads to severe plastic deformation and phase transformation of the original grains, ultimately resulting in the formation of a non-crystalline hardened layer [57,58]. When comparing the results after UVDC processing to those after DC processing, there are two primary reasons for the occurrence of the white layer phenomenon on the workpiece subsurface. On the one hand, the difference in cutting speed is one of the main reasons. The cutting speed during DC processing is a constant 1 m/min, while the cutting speed during UVDC processing is time-varying, with a maximum cutting speed that can reach nearly 40 m/min at a vibration frequency of 103 kHz. Although the cutting time of UVDC in one vibration cycle is only 2 μs, the instantaneous high-speed cutting causes the cutting stress and heat to reach sufficient conditions for the phase transformation of HEAs [59,60]. On the other hand, cutting stability is another crucial factor in the occurrence of the white layer

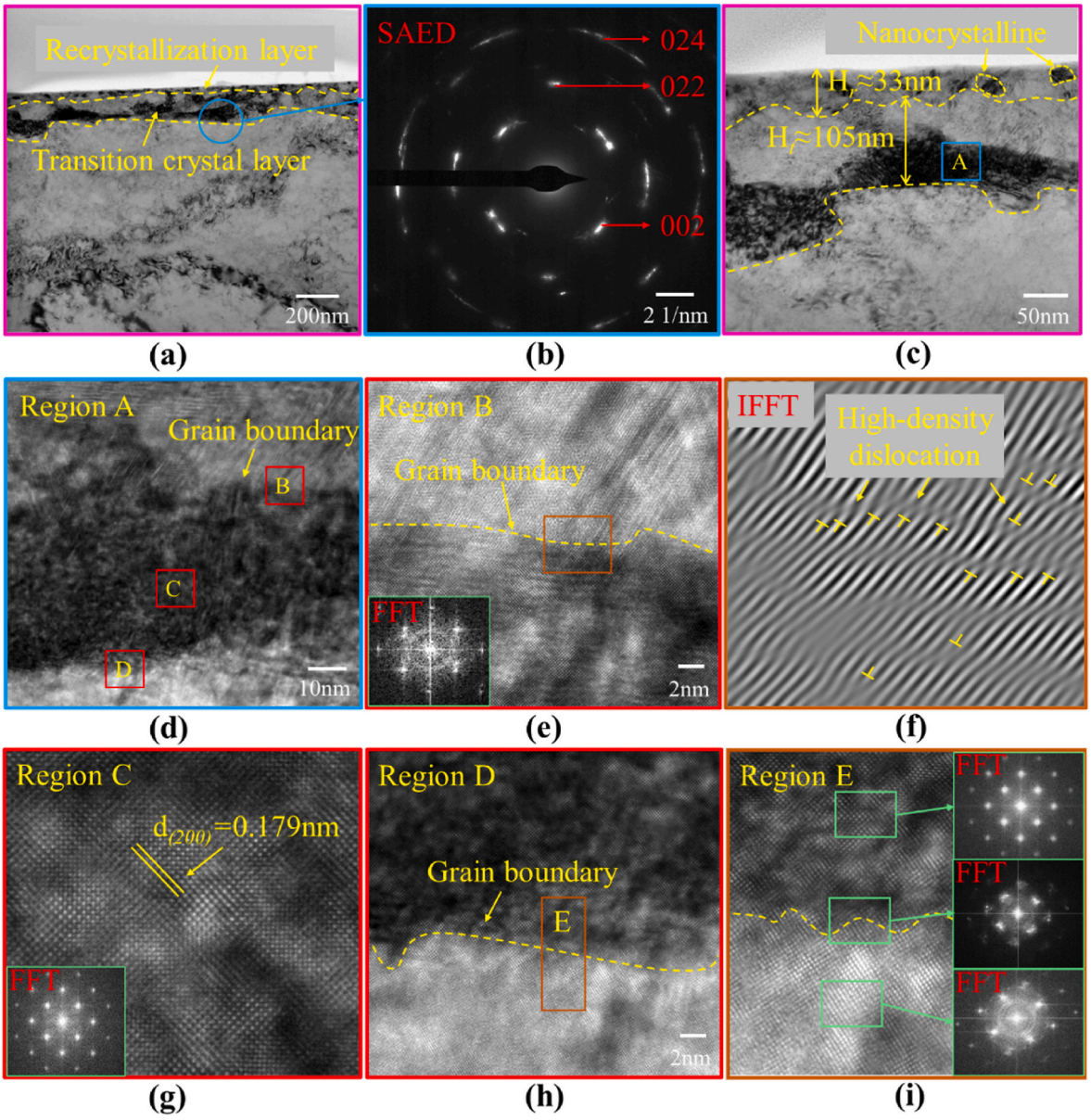

Fig. 11. Microstructure characteristics of the subsurface transition-crystal layer for the machined workpiece after UVDC; (a) Microstructure gradient variation; (b) SAED of the selected area in (a); (c) Transition-crystal layer; (d) Region A; (e) Region B; (f) IFFT pattern in Region B; (g) Region C; (h) Region D; (i) Region E.

phenomenon. Although the DC process is a continuous diamond-cutting process, unstable cutting conditions still make it difficult to distribute heat and stress uniformly, which has been previously verified by research on surface topography. Furthermore, the presence of the amorphous white layer indicates that the surface hardness after UVDC processing is actually higher than that achieved through DC processing, due to the hardening effect of the surface processing [61,62].

In addition, in Region E, a crystalline state, a crystalline-to-amorphous transition zone, and an amorphous-like state are present, progressing from the inside of the crystal to the grain boundary and then to the outside of the crystal. The FFT diffraction pattern presented in Fig. 9 (i) confirms this progression. In other words, a state approaching amorphousness appears around some crystals in the recrystallized layer after UVDC processing. The reason for this phenomenon may be the rapid changes in shear stress and cutting heat due to continuous variations in instantaneous speed during intermittent cutting. Although high-speed cutting produces significant heat generation and high levels of strain during UVDC machining, the separation between the cutter and the workpiece during one complete vibration period quickly releases cutting heat and residual stress, leading to lower energy penetration compared to DC machining. This process hinders the crystal from achieving uniform energy absorption within the dynamic recrystallization process, ultimately resulting in the emergence of local amorphous phenomena. Additionally, the amorphous phenomena also explain why the uniformity of grain sizes in the SAED pattern of the recrystallized layer is lower than that of the DC processing results in Fig. 9 (b), indicating that the measured area contains amorphous components.

Microstructure characteristics of the transition-crystal layer through DC processing are illustrated in Fig. 10. The recrystallization layer, situated between the transition-crystal layer and the workpiece surface, measures approximately 189 nm in thickness as illustrated in Fig. 10 (a). The diffraction peaks of the rings in the SAED pattern of Fig. 10 (b) indicate that the crystal size in the transition-crystal layer is larger than that in the recrystallization layer. Additionally, compared with Fig. 8(b), the particle uniformity of the crystals in Fig. 10 (b) is lower. In Fig. 10 (c), elongated and large crystals can be observed in the transition-crystal layer, whereas nanocrystalline grains are present in the recrystallized layer.

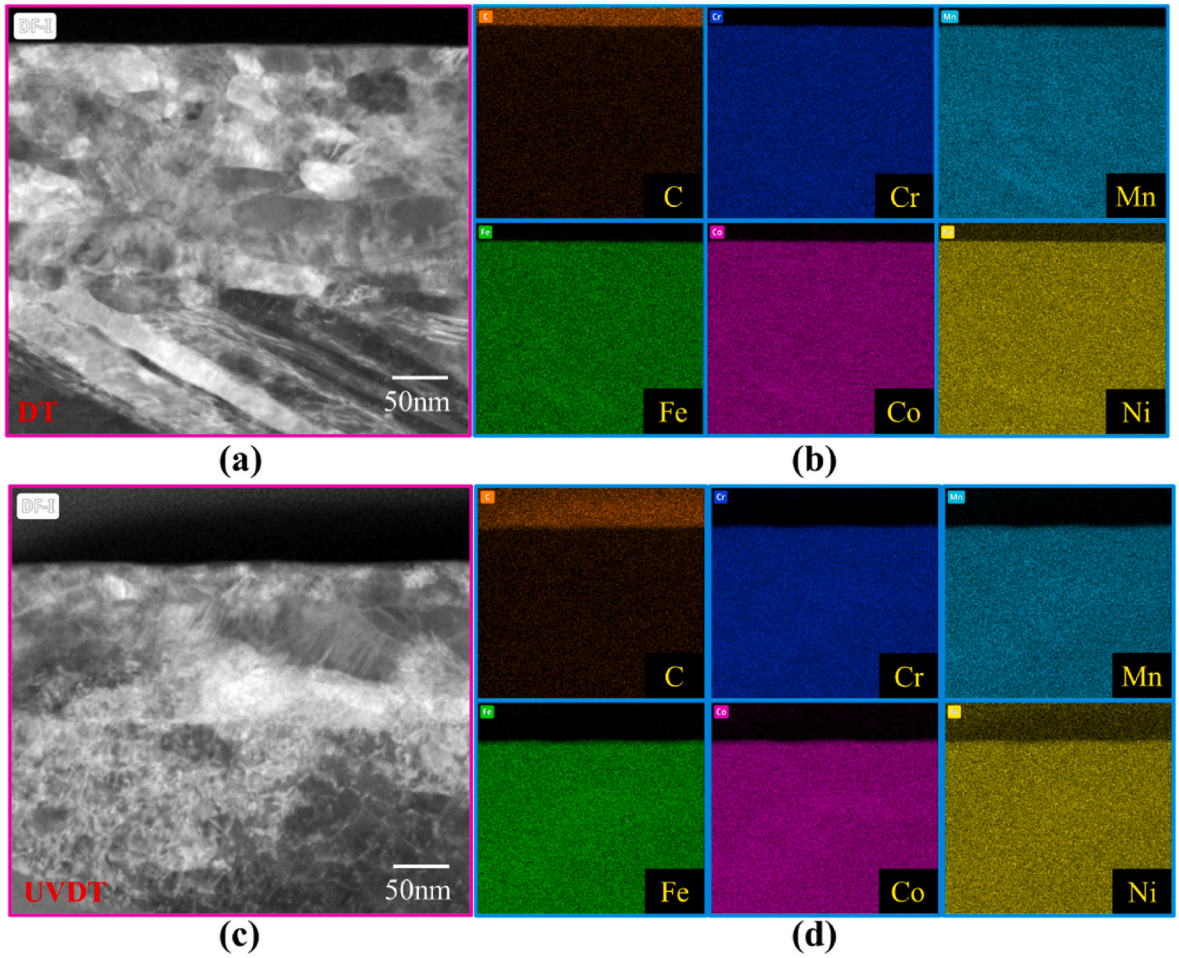

Fig. 12. Elements distribution (CrMnFeCoNi) on the workpiece subsurface after DC and UVDC respectively. (a) Dark field image for subsurface microstructure after DC processing; (b) EDS mapping of region in (a); (c) Dark field image for subsurface microstructure after UVDC processing; (d) EDS mapping of region in (c).

Furthermore, various microstructural features can be observed in Region A through HRTEM analysis, as shown in Fig. 10 (d). In Region B, a significant concentration of stacking faults and twin structures is evident at the grain boundary, which can be verified by FFT patterns presented in Fig. 10 (e). Dense folding structures in the IFFT pattern, as shown in Fig. 10 (f), further verify the existence of high-density stacking faults and dislocations. This feature indicates that high strain rates and local stress concentrations occur in the transition-crystal layer during DC processing. In Region C, stacking faults are also observed at the grain boundary in Fig. 10 (g), indicating that with decreasing energy penetration, crystal slip is hindered, leading to an increased likelihood of stacking faults and twinning. In Region D, a well-ordered crystal arrangement can be observed, with an interplanar spacing of 0.176 nm as shown in Fig. 10 (h). Furthermore, the crystals in the transition-crystal layer after DC processing still retain FCC alloy, as confirmed by the FFT analysis, indicating that the crystal structure of the HEAs remains unchanged after DC process. In Region E, twinning structures can be observed, which are verified by the FFT pattern in Fig. 10 (i).

Fig. 11 shows the microstructural characteristics of the transition-crystal layer through UVDC processing. The thicknesses of the recrystallization layer and the transition-crystal layer are significantly smaller than those after DC processing in Fig. 11 (a). Fig. 11 (b) displays the SAED pattern of the transition-crystal layer. Particle size is larger than that in the recrystallization layer, as evident from Fig. 9 (b). Furthermore, the grain size in the transition-crystal layer is larger than that after DC processing, as demonstrated by Fig. 10 (b). In Fig. 11 (c), the thickness of the recrystallization layer is about 33 nm, and the thickness of the transition-crystal layer is about 105 nm after UVDC processing. The sum of their thicknesses is lower than the thickness of the 189 nm recrystallization layer after DC cutting. This phenomenon indicates that the affecting range of energy penetration of UVDC processing along the cutting depth direction is smaller than the affecting range of DC processing.

In Region A, microstructural features observed at various positions within the crystal are visible in Fig. 11 (d). In Region B, the grain boundaries of crystals after UVDC processing appear as smooth low-angle boundaries, as illustrated in Fig. 11 (e). This is in contrast with the pronounced high-angle grain boundaries observed between adjacent grains after DC processing, shown in Fig. 10 (e). It shows that the grain boundary energy in the transition-crystal layer is smaller. This phenomenon provides evidence from a different perspective that the depth of subsurface evolution after UVDC is shallower than that resulting from DC processing. Additionally, high-density edge dislocations and folding-type stacking faults are observed at grain boundaries through IFFT pattern analysis, as exemplified in Fig. 11 (f). In Region C, there is a regular arrangement of atoms inside the crystal, exhibiting an interplanar spacing of 0.179 nm as illustrated in Fig. 11 (g). In Region D, crystalline structures are visible at the grain boundaries adjacent to the matrix within the transition-crystal layer, as demonstrated in Fig. 11 (h). In Region E, the transition from a crystalline state to a transitional-crystal state, and finally to an unordered state, can be observed from the interior of the crystal to the grain boundary and then to the exterior of the crystal. This pattern is similar to the crystal characteristics observed in the recrystallized layer in Fig. 9 (i). Moreover, after UVDC

processing, an unordered state forms around the crystal, which contrasts with the close proximity observed between adjacent crystals following DC processing.

In addition, Fig. 12 illustrates the distribution of elements on the subsurface of the workpiece following mechanical fabrication. After DC processing, a recrystallization layer consisting of nanocrystal grains and a transition-crystal layer composed of elongated grains are evident in the measurement area depicted in the dark field image of Fig. 12 (a). Utilizing EDS mapping, Fig. 12 (b) reveals a uniform distribution of elements, including iron, cobalt, nickel, chromium, manganese, and oxygen, corresponding to the region shown in Fig. 12 (a). After UVDC processing, the same EDS mapping method is applied, and the results are displayed in Fig. 12 (c) and 12 (d). These findings demonstrate that the distribution of elemental atoms remains uniform and consistent after both DC and UVDC processing.

4.3. Chips formation features

Information on chip morphology characteristics can be further discussed and the influence of different manufacturing technologies on the workpiece finish can be obtained. Fig. 13 shows the features of chip morphology after DC processing. Discontinuous and fragmented chips can be observed in Fig. 13(a), indicating that the HEAs exhibit poor ductility and are prone to forming shattered chips through direct DC processing. For the free surface of chips in Region A, uneven jagged chips can be found in Fig. 13(b) and (c). The reason for the occurrence of these jagged structural features is mainly because of the shear deformation of the chips during cutting [62,63]. Also, in Region A-1, the flake structures with different heights and uneven thicknesses on the free surface of the chip prove the processing instability of HEAs for DC technology. In Region A-2, the edges of the chips are micro-teethed.

In addition, for the chip bottom in Region B in Fig. 13(e)–(i), the obvious fragmented fracture can be discovered on the chip right side. In Region B-1, the chip thickness at the fracture section changes from narrow to wide because the undeformed chip thickness gradually increases during the cutting process of the arc-shaped diamond tool along transverse feeding. The changing characteristics of the chip thickness explain the reason why the fragmented cracks are generated on the right side of the chip. As the thickness of the undeformed chip grows, the cutting energy required to remove material in this area exceeds the energy threshold for the critical fracture strength of HEAs, leading to the generation of cracks [35]. Furthermore, once these generated cracks are not removed along with the chips, they can expand onto the workpiece surface and damage the surface as illustrated in Fig. 4. The appearance of numerous cracks indicates that the cutting stability of HEAs workpieces using DC technology is poor. Observed through local magnification in Fig. 13 (i), the material slippage occurs along the shear direction at the fracture section. The material slip indicates that although the cutting stability of DC machining HEAs is not satisfactory, the shear removal of materials is still a plastic deformation process. In Region B-2, micro-fractures at the chip edge can be observed. Also, the tearing characteristic appears at the fracture edge through partial magnification

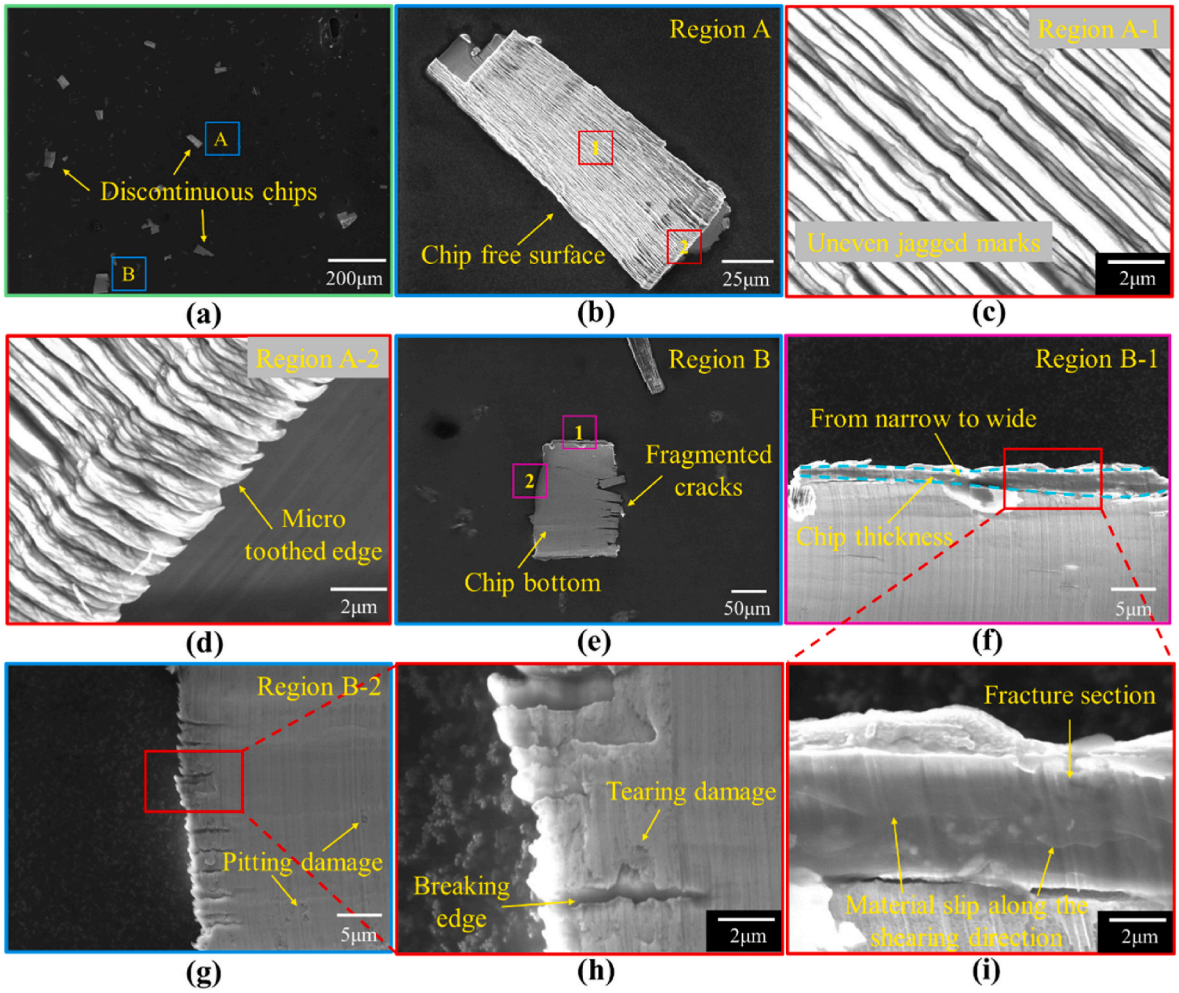

Fig. 13. Chips topography features after DC machining. (a) Overall chip morphology; (b)–(d) Free surface characteristics of chips; (e)–(i) Characteristics of the chip bottom.

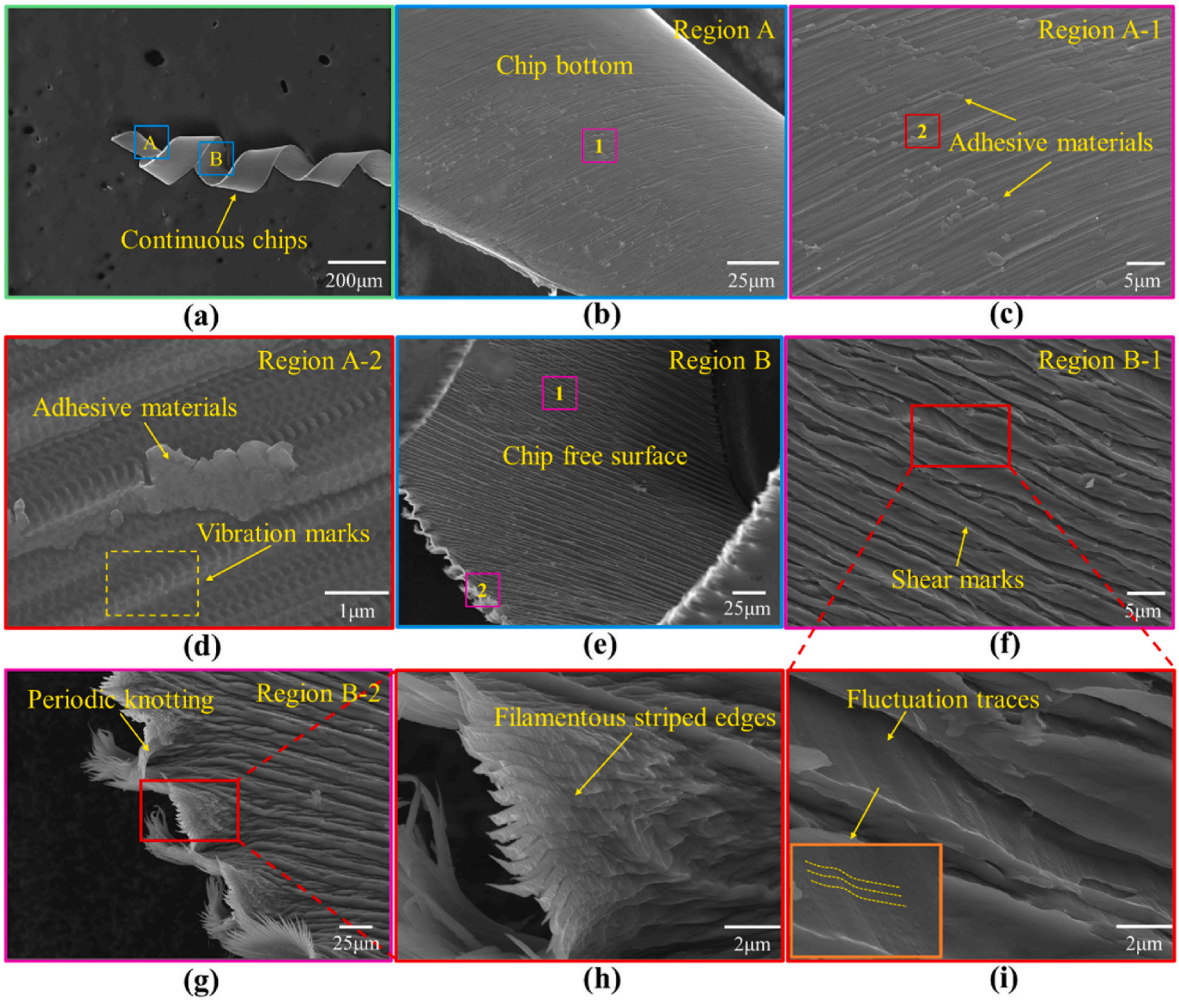

Fig. 14. Chips topography features after UVDC machining. (a) Overall chip morphology; (b)–(d) Characteristics of the chip bottom; (e)–(i) Free surface characteristics of chips.

observation. Tearing damage at the narrow end of the chip is reflected on the surface because the tool moving in the feed direction is no longer a cutting material in this area [64]. This damage feature at the bottom of the chip is one of the reasons why the HEA workpiece has poor surface quality after DC machining.

Fig. 14 displays the features of chip morphology after UVDC processing. The chip maintains a continuous and smooth overall shape in Fig. 14 (a), indicating that the machining stability of intermittent cutting HEAs is significantly improved compared with the DC machining results. Region A shows the characteristics of the chip bottom in Fig. 14(b)–(d). Different from the smooth chip bottom after DC processing, there are adhesive materials and residual vibration marks at the chip bottom after UVDC processing in Regions A-1 and A-2. The formation of attached materials can be associated with micro burrs resulting from vibrational cutting. These burrs can melt and adhere to the chip bottom because of the intense pressure and strong friction at the tooltip. Additionally, the formation of residual vibration marks is primarily caused by the arc-like cutting trajectory. The residual marks on the chips can be mapped with those on the surface as illustrated in Figs. 6(e) and Fig. 14 (d).

Fig. 14(e)–(i) display the features of the chip-free surface in Region B. In Region B-1, the shear marks on the free surface after UVDC processing are more localized and flatter, in contrast to the dense and uneven jagged marks observed after DC processing. Furthermore, fluctuation traces can be observed by magnifying local shear marks. These tiny fluctuation traces along the shear direction are formed by the frequent impact of the diamond tool on the chip during intermittent cutting. In Region B-2, the chip edges show a periodic knotting phenomenon, which is different from the relatively regular chip edges after DC processing. Additionally, each knot has a large number of filamentous striped edges which are formed by each vibration impact. The width of each stripe indicates the extent of cutting influence during a single vibration cycle.

4.4. Tool wear

Fig. 15 illustrates the wear on diamond tools after processing HEA workpieces, following a cutting area of 10 mm^2 and a cutting distance of 5 m approximately, using DC and UVDC technologies respectively. After DC processing, the overall characteristics of the machining tool can be observed as illustrated in Fig. 15 (a). In Region A, the cutting edge between the rake face and the flank face has been severely worn in Fig. 15 (b). The wear width is approximately 4.26 μm. This result indicates that diamond tools are incompatible with directly cutting HEAs since the tool wears too quickly even over a very short cutting distance. Additionally, in Region A-1, built-up edges are discernible on the worn cutting-edge profile, as depicted in Fig. 15 (c). Moreover, because built-up edges are typically harder than that of the original workpiece material due to the machining hardening effect, built-up edges on the cutting edge can serve as substitutes for the cutting tool during machining. This substitution results in a decline in surface quality and heightened surface damage. The rapid deterioration of diamond tools and the presence of built-up edges are major factors that hinder DC machining technology

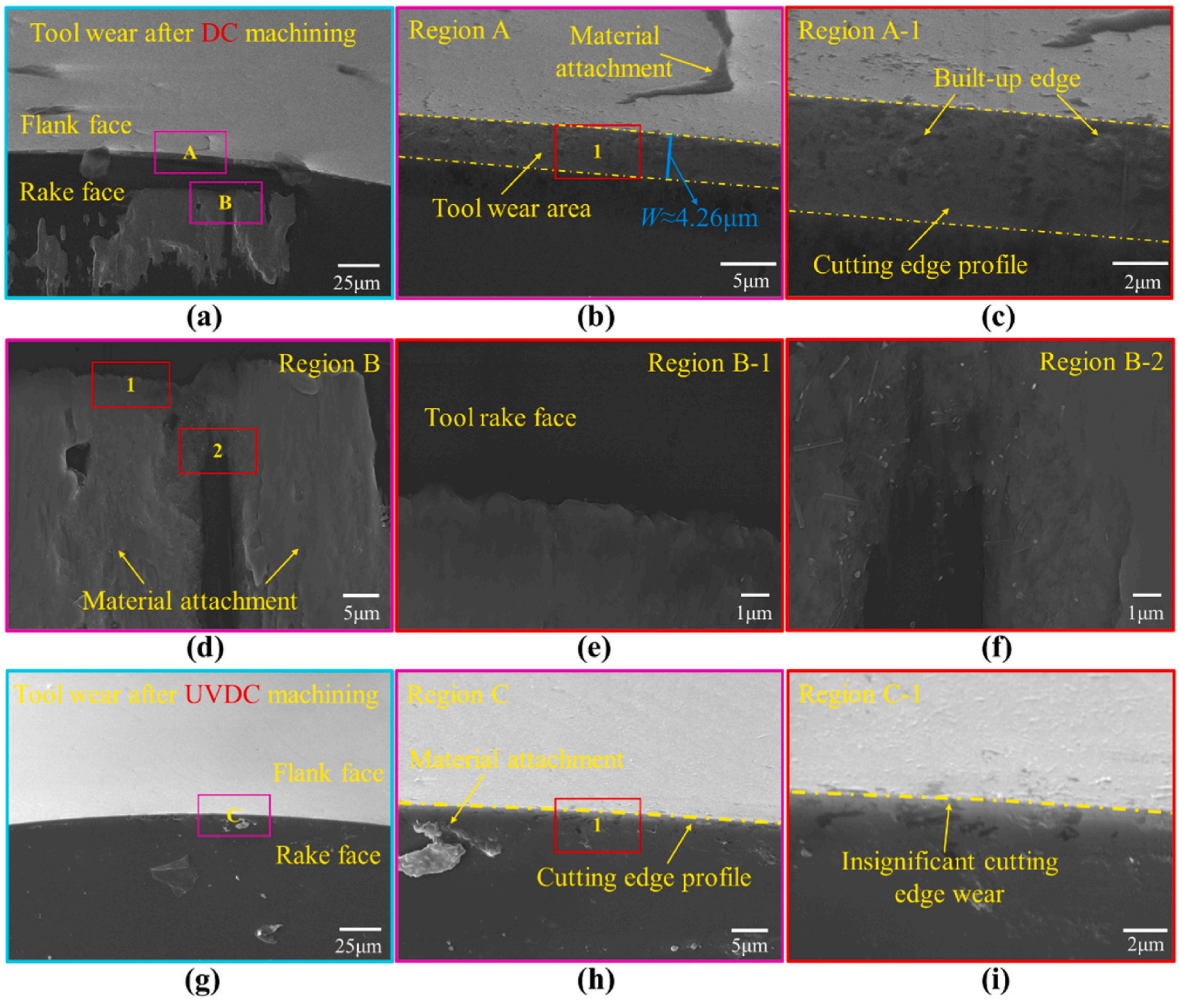

Fig. 15. The diamond tool wear after DC and UVDC machining respectively. (a)–(f) tool wear morphology after DC machining; (g)–(i) tool wear morphology after UVDC machining.

from achieving high-precision surface manufacturing on HEA workpieces. In Region B, a significant amount of material adheres to the rake face, as illustrated in Fig. 15(d)–(f). This material attachment occurs primarily because the chips in the second deformation zone undergo partial melting under conditions of high temperature and pressure extrusion because of intense friction, leading them to stick to the rake face [45,65].

After UVDC processing, the overall characteristics of the machining tool can be observed in Fig. 15 (h). In Region C, unlike the rapid wearing observed on the cutter profile after DC processing, a distinct cutting-edge profile with insignificant wear can be seen in Fig. 15(h)and(i). This phenomenon indicates that UVDC processing technology can inhibit tool wear and extend its lifespan when manufacturing HEA workpieces. During vibrational cutting, the detachment of the cutter and the workpiece allows cutting heat to dissipate, thereby reducing the likelihood of chemical wear. Additionally, the tool reciprocates with high-frequency vibration cutting at 100 kHz, resulting in an actual cutting time of only 20%–40% per cycle, namely 2–4 μs. These brief contacts allow the diamond tool to be further secured and reduce the possibility of damage. Furthermore, when coolant is continuously sprayed, a defensive film can form on the cutting edge during the separation process, providing additional protection for the tool.

4.5. Discussion on cutting mechanism

To thoroughly analyze the benefits of UVDC processing technology in inhibiting surface and subsurface damage during the manufacturing of HEA workpieces, the material removal mechanism with and without ultrasonic vibration assistance is comprehensively discussed and summarized based on previous research content. Fig. 16 illustrates the differences in HEA materials after using DC and UVDC technologies, highlighting the changes from macroscopic surface features to microscopic subsurface evolution. When a diamond tool directly cuts the HEA workpiece, the concentration of instantaneous shear stress and thermal stress leads to material fracture and strong friction marks on the workpiece surface, resulting in significant damage. This is due to the low plastic deformation and poor thermal conductivity of HEA materials. However, UVDC processing technology induces high-frequency, low-amplitude intermittent periodic simple-harmonic vibrations in the diamond tool, which effectively alleviates and evenly distributes the thermal and shear stresses on the workpiece being processed. This improves the surface integrity of the HEA workpiece.

For diamond tool wear features, due to being rich in active transition metal elements, direct cutting of HEA materials induces catastrophic wear even if very short machining distances are performed, thereby aggravating surface damage. During UVDC processing, the high-frequency intermittent cutting characteristics enable the tool and workpiece to undergo instantaneous cutting and separation. In each cycle, the effective cutting time is only 2–4 μs. This process helps maintain the sharpness of the cutting edge and extends the tool lifespan, thereby enhancing the precision of workpiece manufacturing. Additionally, the discontinuous and fragmented chip morphology indicates

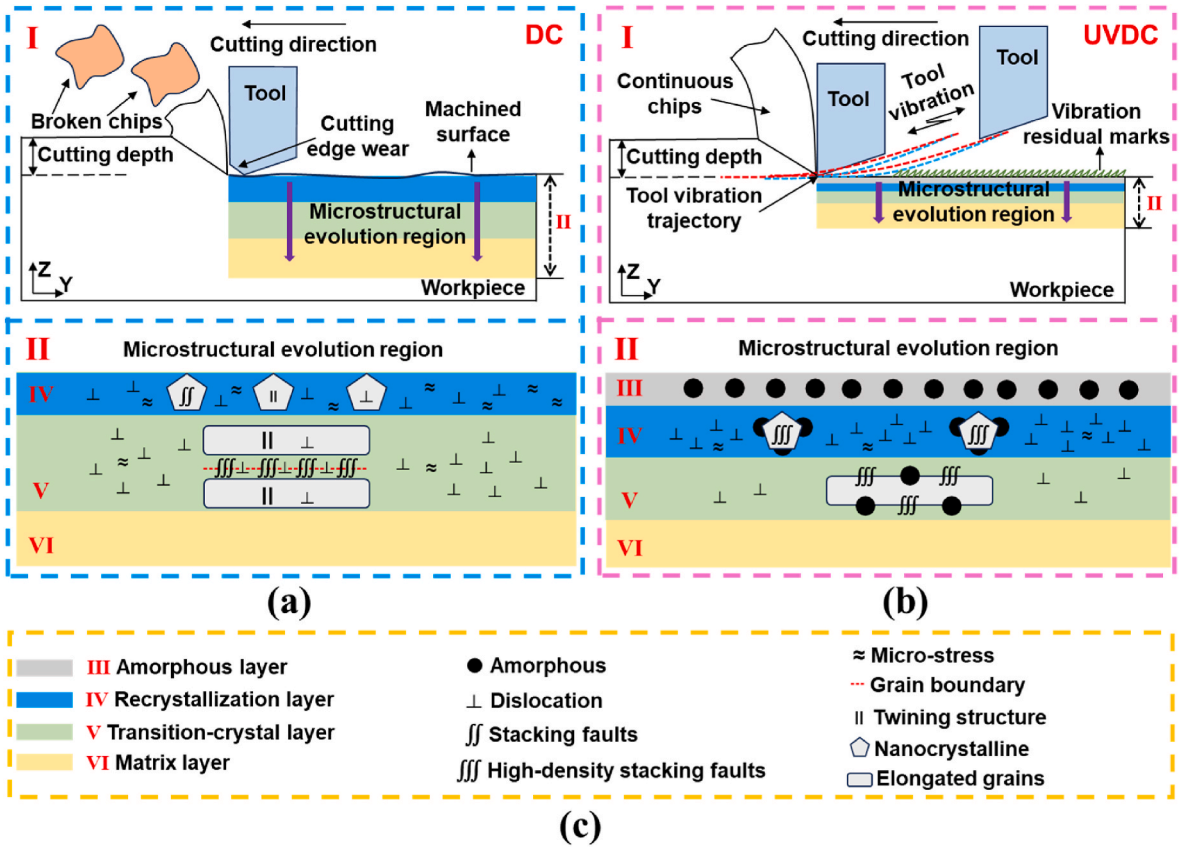

Fig. 16. Schematic diagram of the material removal mechanism of HEA workpiece with or without ultrasonic vibration assistance. (a) After DC machining; (b) after UVDC machining; (c) the meaning of different symbols.

the poor machinability of HEA workpieces when using DC. The presence of adiabatic shear marks further confirms the instability of the cutting process. In contrast, the periodic dynamic stress changes characteristic of UVDC technology effectively reduce internal shear and interface friction effects, forming smooth and continuous chips.

Furthermore, a comprehensive comparison of subsurface microstructure evolution characteristics can provide deeper insights into the manufacturing mechanism of high-frequency intermittent cutting. As shown in Fig. 16, the range of gradient changes after UVDC processing is significantly smaller than that observed after DC processing based on the summary of experimental phenomena, indicating that vibrational cutting can mitigate subsurface damage. The periodic separation of the diamond tool from the workpiece releases part of the stresses that would otherwise penetrate into the subsurface, which reduces the likelihood of distortion in the original crystal structure of the matrix compared to a continuous cutting process. Additionally, the microstructural evolution areas of the two processing technologies can be primarily categorized into the recrystallization layer, transition-crystal layer, and matrix layer. The amorphous white layer appears below the workpiece surface after UVDC processing, suggesting a more uniform distribution of mechanical and thermal stress during high-frequency vibration cutting. In the recrystallized layer, nanocrystals exhibit dislocations, stacking faults, and twins after DC, whereas nanocrystals primarily show high-density stacking faults after UVDC, indicating that intermittent cutting can enhance the plastic deformation of HEA workpiece materials. In the transition-crystal layer, DC processing results in a large number of elongated grains, with high-density stacking faults and twins coexisting at the grain boundaries. UVDC processing reduces the number of elongated grains and decreases the density of the stacking fault structure.

5. Conclusion

This work focuses on a comprehensive understanding of the material removal mechanism of ultraprecision surface formation to inhibit damages for high-entropy alloys (HEAs) using high-frequency ultrasonic vibration-assisted diamond cutting (UVDC) technology. Machinability advantages are obtained based on diverse investigations and comparisons by phenomenological characteristics from macroscopic overall surface topography to microscopic subsurface atomic changes, including workpiece surface, subsurface features, chip morphology, and tool damage in cutting with and without high-frequency ultrasonic vibration assistance. The important conclusions are as follows.

(1) Compared with the continuous diamond cutting (DC) HEAs in the stable processing results, the surface roughness after UVDC processing has been significantly improved from 29 nm to 7 nm. Furthermore, strong friction marks and surface fracture damage can be effectively suppressed because the intermittent cutting process can improve the plastic deformation capacity and heat dissipation capacity during the removal of the materials. In this process, residual vibration marks with a height of about 17 nm are left on the surface of the workpiece due to the diamond tool performing an arc-like movement trajectory.
(2) Among the characteristics of the microstructure evolution, impact damage of subsurface deformation after UVDC processing is less than that after DC processing since the cyclic disconnection between the tool and the HEAs decreases the possibility of severe deformation of the matrix grains induced by continuous stress accumulation.
(3) Compared with the discontinuous broken chips after DC machining, the chips after UVDC processing are continuous and

smooth, indicating that high-frequency intermittent cutting improves machining stability and the plastic deformation ability during materials removal.

(4) Diamond tools are not suitable for direct cutting of HEAs because the tools wear too quickly even within short cutting distances in the experiments. In contrast, a distinct cutting-edge profile with insignificant wear can be observed after UVDC processing, indicating that intermittent cutting can inhibit tool wear and prolong its durability. The wear reduction of diamond tools is an important reason for reducing surface and subsurface damage to HEAs workpieces.

CRediT authorship contribution statement

Yintian Xing: Writing – review & editing, Writing – original draft, Software, Methodology, Investigation, Formal analysis, Data curation, Conceptualization. **Yue Liu:** Software, Investigation, Formal analysis, Data curation. **Yuhan Li:** Formal analysis, Data curation. **Tengfei Yin:** Software, Investigation. **Denghui Li:** Methodology, Software. **Changxi Xue:** Methodology, Data curation. **Wai Sze Yip:** Validation, Software, Data curation, Conceptualization. **Suet To:** Supervision, Resources, Project administration, Funding acquisition.

Data availability

Data will be made available on request.

Declaration of competing interest

The authors declare that they have no known competing financial interests or personal relationships that could have appeared to influence the work reported in this paper.

Acknowledgments

The work described in this paper was partially supported by grant from General Research Fund from the Research Grants Council of the Hong Kong Special Administrative Region (Grant number PolyU15221322); the major project (Project No.: U19A20104) and young scientist fund (Project No.: 52205498/K-ZGFT) of National Natural Science Foundation of China; Shenzhen Science and Technology Program (Project No.: JCYJ20210324131214039); China Postdoctoral Science Foundation (2024M752743); Science and Technology Research Project of Education Department of Jilin Province (JJKH20240919KJ). The authors also would like to thank the financial support from the State Key Laboratory of Ultra-precision Machining Technology and the Research Committee of The Hong Kong Polytechnic University.

References

[1] Zhang SJ, Zhou YP, Zhang HJ, Xiong ZW, To S. Advances in ultra-precision machining of micro-structured functional surfaces and their typical applications. Int J Mach Tool Manufact 2019;142:16–41.
[2] Yuan JL, Lyu BH, Hang W, Deng QF. Review on the progress of ultra-precision machining technologies. Front. Mech. Eng. Prc. 2017;12:158–80.
[3] Zhang GQ, Ma YT, Luo T, Cao SK, Huang ZJ. Fabrication of hierarchical micro-groove structures by vibration assisted end fly cutting. J Mater Process Technol 2023;322:118164.
[4] George EP, Raabe D, Ritchie RO. High-entropy alloys. Nat Rev Mater 2019;4:515–34.
[5] Fu Y, Li J, Luo H, Du CW, Li XG. Recent advances on environmental corrosion behavior and mechanism of high-entropy alloys. J Mater Sci Technol 2021;80:217–33.
[6] Guo J, Zhang JG, Pan YN, Kang RK, Namba Y, Shore P, Yue XB, Wang BR, Guo DM. A critical review on the chemical wear and wear suppression of diamond tools in diamond cutting of ferrous metals. Int J Extrem Manuf 2020;2:012001.
[7] Huang ZY, Dai YQ, Li Z, Zhang GQ, Chang CT, Ma J. Investigation on surface morphology and crystalline phase deformation of Al80Li5Mg5Zn5Cu5 high-entropy alloy by ultra-precision cutting. Mater Des 2020;186:108367.
[8] Yang ZC, Zhu LD, Zhang GX, Ni CB, Lin B. Review of ultrasonic vibration-assisted machining in advanced materials. Int J Mach Tool Manufact 2020;156:103594.
[9] Xing YT, Liu Y, Yin TF, Li DH, Sun ZW, Xue CX, Yip WS, To S. Magnetic and ultrasonic vibration dual-field assisted ultra-precision diamond cutting of high-entropy alloys. Int J Mach Tool Manufact 2024;202:104208.
[10] Yuan ZJ, Xiang DH, Peng PC, Zhang ZQ, Li BH, Ma MY, Zhang ZP, Gao GF, Zhao B. A comprehensive review of advances in ultrasonic vibration machining on SiCp/Al composites. J Mater Res Technol 2023;24:6665–98.
[11] Song Y, Nezu K. Tool wear control in single-crystal diamond cutting of steel by using the ultra-intermittent cutting method. Int J Mach Tool Manufact 2009;49:339–43.
[12] Niu QL, Rong J, Jing L, Gao H, Tang SW, Qiu XY, Liu LP, Wang XH, Dai FP. Study on force-thermal characteristics and cutting performance of titanium alloy milled by ultrasonic vibration and minimum quantity lubrication. J Manuf Process 2023;95:115–30.
[13] Xiao M, Sato K, Karube S, Soutome T. The effect of tool nose radius in ultrasonic vibration cutting of hard metal. Int J Mach Tool Manufact 2003;13:1375–82.
[14] Xing Y, Liu Y, Yang C, Xue C. Roughness model of an optical surface in ultrasonic assisted diamond turning. Appl Opt 2020;59:9722–33.
[15] Chen WX, Zhang X. Investigation on the cutting mechanism of SiCp/Al composites in ultrasonic elliptical vibration machining. Int J Adv Manuf Technol 2022;120:4707–22.
[16] Zhang XY, Peng ZL, Wang DY, Liu LB. Theoretical analysis of cooling mechanism in high-speed ultrasonic vibration cutting interfaces. Int J Therm Sci 2023;184:108033.
[17] Pan YN, Kang RK, Bao Y, Yin S, Dong ZG. Study on tool wear mechanism of single-crystal diamond in ultrasonic vibration elliptical cutting of tungsten heavy alloy. Wear 2020;516:204616.
[18] Zhang XQ, Huang R, Wang Y, Liu K, Deng H, Neo DWK. Suppression of diamond tool wear with sub-millisecond oxidation in ultrasonic vibration cutting of steel. J Mater Process Technol 2022;299:117320.
[19] Nath C, Rahman M. Effect of machining parameters in ultrasonic vibration cutting. Int J Mach Tool Manufact 2008;48:965–74.
[20] Wang JJ, Liao WH, Guo P. Modulated ultrasonic elliptical vibration cutting for ductile-regime texturing of brittle materials with 2-D combined resonant and non-resonant vibrations. Int J Mech Sci 2020;170:105347.
[21] Duan JW, Zou P, Wang AQ, Wei SY, Fang R. Research on three-dimensional ultrasonic vibration-assisted turning cutting force. J Manuf Process 2023;91:167–87.
[22] Patil S, Joshi S, Tewari A, Joshi SS. Modelling and simulation of effect of ultrasonic vibrations on machining of Ti6Al4V. Ultrasonics 2014;54:694–705.
[23] Wang H, Yang GL, Su H, Dong ZG, Guo XG, Bao Y, Zhang PF. Insight into surface formation mechanism during ultrasonic elliptical vibration cutting of tungsten alloy by scratching experiment and molecular dynamics. Tribol Int 2024;191:109088.
[24] Wang JP, Zhang GQ, Chen N, Zhou MH, Chen YB. A review of tool wear mechanism and suppression method in diamond turning of ferrous materials. Int J Adv Manuf Technol 2021;113:3027–55.
[25] Huang S, Liu X, Chen FZ, Zheng HX, Yang XL, Wu LB, Song JL, Xu WJ. Diamond-cutting ferrous metals assisted by cold plasma and ultrasonic elliptical vibration. Int J Adv Manuf Technol 2016;85:673–81.
[26] Sui H, Zhang XY, Zhang DY, Jiang XG, Wu RB. Feasibility study of high-speed ultrasonic vibration cutting titanium alloy. J Mater Process Technol 2017;247:111–20.
[27] Maurotto A, Muhammad R, Roy A, Silberschmidt VV. Enhanced ultrasonically assisted turning of a β-titanium alloy. Ultrasonics 2013;53:1242–50.
[28] Zhang JG, Yuan HX, Feng LQ, Zhang JJ, Chen X, Xiao JF, Xu JF. Enhanced machinability of Ni-based single crystal superalloy by vibration-assisted diamond cutting. Precis Eng 2023;79:300–9.
[29] Yu TB, Yang XZ, An JH, Yu XM, Zhao J. Material removal mechanism of two-dimensional ultrasonic vibration assisted polishing Inconel718 nickel-based alloy. Int J Adv Manuf Technol 2018;26:657–67.
[30] Bai JX, Xu ZW, Qian LM. Precision-improving manufacturing produces ordered ultra-fine grained surface layer of tungsten heavy alloy through ultrasonic elliptical vibration cutting. Mater Des 2022;220:110859.
[31] Zhao QX, Guo XG, Wang H, Yin S, Kang RK, Dong ZG, Bao Y. Effects of ultrasonic vibration cutting trajectories on chip formation of tungsten alloys. J Manuf Process 2023;92:147–56.
[32] Zhang XQ, Huang R, Liu K, Kumar AS, Deng H. Suppression of diamond tool wear in machining of tungsten carbide by combining ultrasonic vibration and electrochemical processing. Ceram Int 2018;44:4142–53.
[33] Zhang JJ, Han L, Zhang JG, Liu HY, Yan YD, Sun T. Brittle-to-ductile transition in elliptical vibration-assisted diamond cutting of reaction-bonded silicon carbide. J Manuf Process 2019;45:670–81.
[34] Zhang C, Meng FW, Liang YD, Yu TB. Surface integrity study of ZrO2 ceramic for ultrasonic vibration-assisted polishing processing. Ceram Int 2024;50:2259–70.
[35] Xing YT, Xue CX, Liu Y, Du HH, Yip WS, To S. Freeform surfaces manufacturing of optical glass by ultrasonic vibration-assisted slow tool servo turning. J Mater Process Technol 2024;324:118271.
[36] Xing YT, Liu Y, Li C, Yang C, Xue CX. Ductile-brittle coupled cutting of a single-crystal silicon by ultrasonic assisted diamond turning. Opt Express 2021;29:23847–63.
[37] Zhang JG, Zhang JJ, Liu CL, Chen X, Xiao JF, Xu JF. Machinability of single crystal calcium fluoride by applying elliptical vibration diamond cutting. Precis Eng 2020;66:306–14.
[38] Wang QG, Cong WL, Pei ZJ, Gao H, Kang RK. Rotary ultrasonic machining of potassium dihydrogen phosphate (KDP) crystal: an experimental investigation on surface roughness. J Manuf Process 2009;11:66–73.

[39] Ma SY, Lu YJ, Li XH, Lai JJ, Zhang JG, Chen X, Xiao JF, Xu JF. Investigation on the machinability of polycrystalline ZnSe by elliptical vibration diamond cutting. Opt Express 2024;32:482–98.
[40] Saito H, Jung HJ, Shamoto E, Wu TC, Chien JT. Mirror surface machining of high-alloy steels by elliptical vibration cutting with single-crystalline diamond tools: influence of alloy elements on diamond tool damage. Precis Eng 2017;49:200–10.
[41] Chen JY, Jin TY, Luo XC. Key machining characteristics in ultrasonic vibration cutting of single crystal silicon for micro grooves. Adv Manuf 2019;7:303–14.
[42] Wang H, Kang RK, Bao Y, Wang KX, Guo XG, Dong ZG. Microstructure evolution mechanism of tungsten induced by ultrasonic elliptical vibration cutting at atomic/nano scale. Int J Mech Sci 2023;253:108397.
[43] Peng ZL, Zhang XY, Liu LB, Xu GT, Wang G, Zhao MH. Effect of high-speed ultrasonic vibration cutting on the microstructure, surface integrity, and wear behavior of titanium alloy. J Mater Res Technol 2023;24:3870–88.
[44] Luo L, Wu JZ, Gao PF, Chen FJ. Mechanism and deformation behavior of elliptical vibration-assisted cutting of FeNiCrCoAl high entropy alloy. Mater Today Commun 2024;39:108992.
[45] Zhang L, Hashimoto T, Yan JW. Machinability exploration for high-entropy alloy FeCrCoMnNi by ultrasonic vibration-assisted diamond turning. CIRP Ann - Manuf Technol 2021;70:37–40.
[46] Xing YT, Liu Y, Li C, Yang C, Xue CX. Fabrication of high-precision freeform surface on die steel by ultrasonic-assisted slow tool servo. Opt Express 2021;29:3708–23.
[47] Gaidys R, Dambon O, Ostasevicius V, Dicke C, Narijauskaite B. Ultrasonic tooling system design and development for single point diamond turning (SPDT) of ferrous metals. Int J Adv Manuf Technol 2017;93:2841–54.
[48] Zhang CB, Liang XL, Cheung CF, Wang CJ, Bulla BJ. Theoretical and experimental investigation of ultrasonic cutting kinematics and its effect on chip formation and surface generation in high-frequency ultrasonic vibration-assisted diamond cutting. J Mater Res Technol 2024;30:5662–76.
[49] Li WD, Liaw PK, Gao YF. Fracture resistance of high entropy alloys: a review. Intermetallics 2018;99:69–83.
[50] Liang XL, Zhang CB, Cheung C, Wang CJ, Li KS, Bulla B. Micro/nano incremental material removal mechanisms in high-frequency ultrasonic vibration-assisted cutting of 316L stainless steel. Int J Mach Tool Manufact 2023;191:104064.
[51] He CL, Yan JW, Wang SQ, Zhang S, Chen G, Ren CG. A theoretical and deep learning hybrid model for predicting surface roughness of diamond-turned polycrystalline materials. Int J Extrem Manuf 2023;5:035102.
[52] He CL, Zong WJ, Xue CX, Sun T. An accurate 3D surface topography model for single-point diamond turning. Int J Mach Tool Manufact 2018;134:42–68.
[53] Xu X, Zhang J, Outeiro J, Xu BB, Zhao WH. Multiscale simulation of grain refinement induced by dynamic recrystallization of Ti6Al4V alloy during high speed machining. J Mater Process Technol 2020;286:116834.
[54] Liang XL, Liu ZQ, Wang B. Dynamic recrystallization characterization in Ti-6Al-4V machined surface layer with process-microstructure-property correlations. Appl. Sruf. Sci. 2020;530:147184.
[55] Huang WH, Yan JW. Surface formation mechanism in ultraprecision diamond turning of coarse-grained polycrystalline ZnSe. Int J Mach Tool Manufact 2020;153:103554.
[56] Su RZ, Neffati D, Zhang YF, Cho J, Li J, Wang HY, Kulkarni Y, Zhang XH. The influence of stacking faults on mechanical behavior of advanced materials. Mat. Sci. Eng. A- Struct. 2021;803:140696.
[57] Hosseini SB, Klement U, Yao Y, Ryttberg K. Formation mechanisms of white layers induced by hard turning of AISI 52100 steel. Acta Mater 2015;89:258–67.
[58] Hosseini SB, Beno T, Klement U, Kaminski J, Ryttberg K. Cutting temperatures during hard turning—measurements and effects on white layer formation in AISI 52100. J Mater Process Technol 2014;214:1293–300.
[59] Arfaoui S, Zemzemi F, Tourki Z. Relationship between cutting process parameters and white layer thickness in orthogonal cutting. Mater Manuf Process 2018;33:661–9.
[60] Bosheh SS, Mativenga PT. White layer formation in hard turning of H13 tool steel at high cutting speeds using CBN tooling. J. Mach. Tool. Manu. 2006;46:225–33.
[61] Zhang FY, Duan CZ, Wang MJ, Sun W. White and dark layer formation mechanism in hard cutting of AISI52100 steel. J Manuf Process 2018;32:878–87.
[62] Guo YB, Sahni J. A comparative study of hard turned and cylindrically ground white layers. Int J Mach Tool Manufact 2004;44:135–45.
[63] Li JM, Zuo YS, Wang Y, Wang YQ, Liu HB, Zhang J, Jiang SW. On the chip formation mechanism when cutting Ti6Al4V with localised supply of liquid nitrogen. J Mater Process Technol 2024;237:118377.
[64] Sun ZW, Zhang T, Li PZ, Wang SJ, To S, Wang HL. Analytical modelling of the trans-scale cutting forces in diamond cutting of polycrystalline metals considering material microstructure and size effect. Int J Mech Sci 2021;204:106575.
[65] Du HH, Wang YD, Li YH, Yin S, Li DH, Yip WS, To S. Improving the machinability of the high-entropy alloy CoCrFeMnNi by in-situ laser-assisted diamond turning. J Mater Res Technol 2023;27:7110–8.